



HAL
open science

Regions of interest (ROI) for future exploration missions to the lunar South Pole

Jessica Flahaut, J. Carpenter, J.-P. Williams, M. Anand, I.A. Crawford, W. van Westrenen, E. Fűri, L. Xiao, S. Zhao

► To cite this version:

Jessica Flahaut, J. Carpenter, J.-P. Williams, M. Anand, I.A. Crawford, et al.. Regions of interest (ROI) for future exploration missions to the lunar South Pole. *Planetary and Space Science*, 2020, 180, pp.104750. 10.1016/j.pss.2019.104750 . hal-02345336

HAL Id: hal-02345336

<https://hal.science/hal-02345336>

Submitted on 7 Dec 2020

HAL is a multi-disciplinary open access archive for the deposit and dissemination of scientific research documents, whether they are published or not. The documents may come from teaching and research institutions in France or abroad, or from public or private research centers.

L'archive ouverte pluridisciplinaire **HAL**, est destinée au dépôt et à la diffusion de documents scientifiques de niveau recherche, publiés ou non, émanant des établissements d'enseignement et de recherche français ou étrangers, des laboratoires publics ou privés.

Regions of Interest (ROI) for future exploration missions to the lunar South Pole

Flahaut J.^{1}, J. Carpenter², J.-P. Williams³, M. Anand⁴, I. Crawford⁵, W. van Westrenen⁶, E. Füri¹, L. Xiao⁷ and S. Zhao⁷.*

1- Centre de Recherches Pétrographiques et Géochimiques (CRPG), CNRS/ Université de Lorraine, 15 rue Notre-Dame des Pauvres, 54500 Vandœuvre-lès-Nancy, France,

2- ESA-ESTEC, Noordwijk, NL,

3- Department of Earth, Planetary, and Space Sciences, University of California, USA,

4- School of Physical Sciences, The Open University, Milton Keynes, UK,

5- Department of Earth and Planetary Sciences, Birkbeck College, University of London, London, UK,

6- Faculty of Earth and Life Sciences, Vrije Universiteit (VU) Amsterdam, NL,

7- Planetary Science Institute, China University of Geosciences, Wuhan, 430074, China.

*Corresponding author: Dr Jessica Flahaut, Centre de Recherches Pétrographiques et Géochimiques, 15 rue Notre-Dame des Pauvres, 54500 Vandœuvre-lès-Nancy, France. Email: jessica.flahaut@univ-lorraine.fr

Abstract

The last decades have been marked by increasing evidence for the presence of near-surface volatiles at the lunar poles. Enhancement in hydrogen near both poles, UV and VNIR albedo anomalies, high CPR in remotely sensed radar data have all been tentatively interpreted as evidence for surface and/or subsurface water ice. Lunar water ice and other potential cold-trapped volatiles are targets of interest

26 both as scientific repositories for understanding the evolution of the Solar System and for exploration
27 purposes. Determining the exact nature, extent and origin of the volatile species at or near the surface
28 in the lunar polar regions however requires *in situ* measurements via lander or rover missions. A
29 number of upcoming missions will address these issues by obtaining *in situ* data or by returning
30 samples from the lunar surface or shallow subsurface. These all rely on the selection of optimal
31 landing sites. The present paper discusses potential regions of interest (ROI) for combined volatile and
32 geologic investigations in the vicinity of the lunar South Pole. We identified eleven regions of interest
33 (including a broad area of interest ($> 200 \text{ km} \times 200 \text{ km}$) at the South Pole, together with smaller
34 regions located near Cabeus, Amundsen, Ibn Bajja, Wiechert J and Idel'son craters), with enhanced
35 near-surface hydrogen concentration ($H > 100 \text{ ppm}$ by weight) and where water ice is expected to be
36 stable at the surface, considering the present-day surface thermal regime. Identifying more specific
37 landing sites for individual missions is critically dependent on the mission's goals and capabilities. We
38 present detailed case studies of landing site analyses based on the mission scenario and requirements
39 of the upcoming Luna-25 and Luna-27 landers and Lunar Prospecting Rover case study. Suitable sites
40 with promising science outcomes were found for both lander and rover scenarios. However, the rough
41 topography and limited illumination conditions near the South Pole reduce the number of possible
42 landing sites, especially for solar-powered missions. It is therefore expected that limited Sun and Earth
43 visibility at latitudes $> 80^\circ$ will impose very stringent constraints on the design and duration of future
44 polar missions.

45 **Keywords**

46 Lunar poles; volatiles; ISRU; water ice; landing sites; GIS

47 **Highlights**

- 48 • There is increasing evidence for cold-trapped volatiles around the South Pole, that are
49 targeted by upcoming lander and rover missions.

- 50 • Several areas of interest identified around the South Pole are suitable for future
51 investigations of both lunar volatiles and regional geology.
- 52 • Case studies illustrate that precise landing site selection is highly mission dependent.
- 53 • Illumination and Earth visibility remain limited in the South Pole region and will
54 strongly impact future mission scenarios.

55 **1. Introduction**

56 For over half a century, scientists have been debating the existence of water ice and other cold-trapped
57 volatiles at the lunar poles (e.g., Watson, 1961; Arnold, 1979; Ingersoll et al., 1992; Feldman et al.,
58 2001; Anand 2010; Paige et al., 2010; Hayne et al., 2015; Li et al., 2018). Because of the low
59 inclination of the Moon’s rotational axis, illumination conditions at the poles are extreme, and regions
60 of permanent shadow exist at latitudes $> 65^\circ$. Areas that never receive direct sunlight (referred to as
61 permanently shadowed regions, PSRs) are invariably cold (~40 K) and considered as possible
62 reservoirs for ice sequestration (Ingersoll et al., 1992; Paige et al., 2010). Multiple evidence from
63 recent orbiter missions seem to confirm the presence of ice and other volatiles inside, but also outside
64 of PSRs, drawing more attention to the lunar poles these last years (e.g., Colaprete et al., 2010; Hayne
65 et al., 2015; Li et al., 2018). Water ice and other volatiles on the Moon are fundamental tracers of
66 dynamical material exchange among different regions of the Solar System (e.g., Lin et al., 2019), but
67 are also key to understanding the Moon’s origin and evolution (e.g., Anand et al., 2014; Lin et al.,
68 2017). In addition, cold-trapped volatiles might represent valuable resources to support future lunar
69 infrastructures and space exploration in general (e.g. Anand et al. 2012; Crawford et al. 2012).

70 A number of studies have been initiated in the past years, making use of the wealth of available remote
71 sensing datasets, to highlight potential regions of interest for future lunar missions aimed at
72 investigating the cold-trapped polar volatiles, with a stronger focus on the South Pole. Situated within
73 the outer portion of the South-Pole Aitken basin, the South Pole offers a unique opportunity to
74 determine the age and the structure of this basin, which is the largest (2600 km diameter) and oldest
75 known impact structure in the Solar System (e.g., Wilhelms et al., 1991; Spudis et al., 1994). Because

76 of this additional scientific benefit of outstanding value, the South Pole tends to be favored compared
77 to the North Pole for upcoming missions, and is the focus of this paper.

78 Lemelin et al. (2014) used a multi-parameter analysis to select optimal landing sites for returning
79 volatile-rich samples from the poles. The authors searched for suitable landing sites where concept 4
80 of the NRC report (2007) “The lunar poles are special environments that may bear witness to the
81 volatile flux over the latter part of solar system history” could be best addressed. They identified the
82 regions with the best chances of containing accessible volatiles as those (1) in permanently shaded
83 regions, (2) with enhanced hydrogen abundances (greater than 150 ppm), (3) maximum annual
84 temperature between 0-54 K, (4) minimum annual temperature between 0-54 K, (5) average annual
85 temperature between 0-130 K, and (6) shallow slopes (shallower than 25 degrees for rover mobility
86 constraints). They found two such sites in the south polar region (Shoemaker and Faustini craters), and
87 two in the north polar region (Peary crater and a region between Hermite and Rozhdestvenskiy W
88 craters). They relaxed the constraints, allowing one of the six criteria to be suboptimal, and identified
89 five additional sites in the south polar region (Haworth, De Gerlache, and Cabeus craters as well as a
90 region between Shoemaker and Faustini craters and the northern portion of Amundsen crater) and
91 three additional sites in the north polar region (Lenard, Hermite and Rozhdestvenskiy W craters).
92 Given that these sites are all located within PSRs, they might however be challenging to access with a
93 solar-powered spacecraft.

94 The same year, a LEAG team (the VSAT – Volatile Specific Action Team) was tasked by NASA to
95 make landing site recommendations for future missions. Largely based on the Lemelin et al. (2014)
96 study, but varying thresholds and adding constraints on the Sun and Earth visibility, the LEAG team
97 proposed regions of interest (ROI) near Cabeus and Shoemaker in the South Pole region. This
98 selection was largely based on the imposed requirement that H abundance, as estimated from the
99 Lunar Prospector Neutron Spectrometer (LPNS) data, had to be above 150 ppm, among other criteria
100 (annual surface temperature >110K, modest slopes <10°, proximity of PSRs (<1km)) (LEAG VSAT,
101 2015).

102 In 2015, an ESA team published a response to the LEAG report (ESA TT ELPM, 2015). The
103 European recommendations in terms of orbiter and lander measurement findings were similar to those
104 of the LEAG report. The ESA study however considered the possibility of combining volatile studies
105 with additional scientific (geologic) investigations. The team proposed to work with an enlarged set of
106 parameters, that account for potential additional science benefits (and hence consider the possibility to
107 fill more science concepts of the NRC report), to define regions of interest near the poles. In particular,
108 relaxing the H abundance threshold to 125 ppm and the need to be within 1 km of a PSRs (which
109 mostly applies to a rover-scenario) resulted in a more extended area available for exploration (ESA TT
110 ELPM, 2015; Flahaut et al., 2016a, b).

111 The present paper describes regions of interest that address multiple science questions such as the
112 nature and distribution of polar volatiles (NRC concept 4), but also the potential to investigate the
113 lunar chronology (NRC science concept 1), lunar interior (NRC concept 2), and the lunar crust
114 diversity (NRC concept 3) (NRC, 2007). Section 2 summarizes the start-of-the art knowledge of the
115 South Pole environment that addresses some challenges anticipated for future lunar missions. The
116 datasets and methods used to define ROIs are listed in Section 3. Given that finding a candidate
117 landing site is very specific to a mission's objectives and design, broad areas of interest are presented
118 in section 4. We then present three detailed landing site analysis case studies based on the
119 characteristics of some planned (or studied) missions to the South Pole: Luna-25, Luna-27 and ESA's
120 Lunar Prospecting Rover (LPR) concept (Section 5). Example traverses along the Shoemaker-Faustini
121 ridge are presented for the rover case study.

122

123 **2. The South Pole environment**

124 The South Pole region is marked by a rough topography, owing to its location on the South Pole
125 Aitken basin (SPA) rim and superimposed impacts (e.g., Wilhems, 1979; Spudis et al., 2008).
126 Elevation ranges from about -8000 to +8000 m with slopes as steep as 80° (Figure 1a, b). Because of

127 this rough topography and the Moon's small axial inclination (1.54°), illumination conditions at the
128 South Pole are extreme (e.g., Bussey et al., 1999; 2010; Noda et al., 2008; Mazarico et al., 2011). Most
129 polar locations receive sunlight for less than 50% of the time, as illustrated by low illumination
130 fraction values (<0.5) on Figure 1c. Lunar Orbiter Laser Altimeter (LOLA) based simulations over
131 long time-periods (several 18.6-year lunar precession cycles) at 240 m/ pixel and down to $\sim 75^\circ$
132 latitude revealed that PSRs extend beyond the expected PSR crater floors and represent a total area
133 exceeding 16,000 km² near the South Pole (e.g., Bussey et al., 2003; Zuber et al., 1997; Margot et al.,
134 1999; McGovern et al., 2013; Mazarico et al., 2011, their figure 8). Still, areas of limited extent that
135 experience nearly-persistent illumination (over 80% of the day on average) were identified near the
136 rims of Shackleton and De Gerlache craters and the connecting ridge in between, but also on the rim of
137 Nobile crater and on the crest of the Malapert Massif (e.g., Fig. 12 of Mazarico et al., 2011; Figure
138 S1). For most of these locations, a small height gain of a solar panel (2 to 10 m) can significantly
139 improve illumination conditions, providing a near-continuous source of power, and making them
140 interesting targets for future exploration missions (e.g., Mazarico et al., 2011; De Rosa et al., 2012;
141 McGovern et al., 2013; Speyerer et al., 2013; Gläser et al., 2014, 2018). The characteristics of these
142 regions are briefly discussed in the next sections, and presented in Figure S2.

143 With average annual surface temperatures as low as 38 K near the lunar South Pole; PSRs are cold
144 enough for cold-trapped volatiles, including water ice, to be present (Zhang and Paige, 2009, Paige et
145 al., 2010; Figure 1g). Data acquired by various remote sensing instruments in orbit around the Moon
146 suggest that water frost is present at the surface or subsurface in some PSRs, and beyond. Surface frost
147 could explain anomalies in Lyman Alpha Mapping Project (LAMP) and LOLA 1064 nm surface
148 albedo, which are rather well correlated, and suggest the presence of 1-10 % water ice (Hayne et al.,
149 2015; Lucey et al., 2014; Fisher et al., 2017; Figure 2a). Many of these locations also exhibit
150 diagnostic near-infrared absorption features of water ice in reflectance spectra acquired by the Moon
151 Mineralogy Mapper (M3) instrument (Li et al., 2018). The LPNS and Lunar Energetic Neutron
152 Detector (LEND) have measured enhanced Hydrogen concentrations around the South Pole, with
153 estimates of 0.3-0.5 wt% Water-Equivalent Hydrogen (WEH) within the uppermost meter of the

154 surface in PSRs (e.g., Feldman et al., 2001; Mitrofanov et al., 2012a; Sanin et al., 2016; Lawrence,
155 2017; Figure 1e,f). Spatially deconvolved neutron data for 12 PSRs yield WEH values in the range of
156 0.2 to ~3 wt%, with an average of 1.4 wt% (Teodoro et al., 2010). Both Deep Impact and M3 Visible
157 Near Infra-Red (VNIR) hyperspectral data show latitudinal variations in the strength of the 3 μm
158 OH/H₂O absorption band (Pieters et al., 2009; Sunshine et al., 2009). However, the nature and origin
159 of the hydrogen-host phase(s) are uncertain. Potential sources of H include comet and asteroid
160 impacts, solar wind implantation, and outgassing from the lunar interior (e.g., Anand et al., 2014);
161 these different contributions could potentially be distinguished based on hydrogen isotope (D/H) ratio
162 measurements (e.g., F \ddot{u} ri and Marty, 2015), either through *in situ* volatile studies or laboratory
163 analyses of returned samples.

164 Spectral analyses of the Lunar Crater Observation and Sensing Satellite (LCROSS) impact plume in
165 Cabeus crater provide tantalizing clues to the nature of some polar volatiles. In addition to $\sim 5.6 \pm 2.9$
166 % water ice in the regolith (by mass), a number of other volatile compounds were observed, including
167 light hydrocarbons, sulfur-bearing species, and carbon dioxide (Colaprete et al., 2010; Gladstone et al.,
168 2010). An opposition effect was also observed in the LRO mini-RF and Arecibo datasets on the floor
169 of Cabeus and interpreted as evidence for the presence of water ice near the surface (Patterson et al.,
170 2017). A same-sense polarization enhancement within the South Pole PSRs with the Clementine bi-
171 static experiment was tentatively interpreted as showing the presence of low-loss volume scatterers,
172 such as water ice (Nozette et al., 1996, 2001). High CPR acquired by the Chandrayaan-1 mini-SAR and
173 the LRO mini-RF are well-correlated with PSRs and might also indicate the presence of discontinuous
174 ice blocks at shallow depths (Spudis et al., 2010b, 2013, 2016; Figure 2a). These observations,
175 however, are not collocated with the predictions of ice stability at both the surface and depth made
176 from Diviner's present-day thermal infrared observations (e.g., Siegler et al., 2015; Figure 2b).
177 Altogether, current observations point to the existence of water ice, and possibly other cold-trapped
178 volatiles (such as carbon monoxide, mercury, and sodium detected in the LCROSS plume, or 'Super-
179 volatiles' – those with vapor pressures much higher than that of water – such as CO₂, CO, CH₄, NH₃,
180 CH₃OH, and H₂S, which may be present as predicted by the temperature range), distributed

181 heterogeneously at varying locations and depths in the polar regolith (e.g., Gladstone et al., 2010;
182 Zhang and Paige, 2011; Hayne et al., 2019).

183

184 **3. Remote sensing datasets**

185 A wealth of remote sensing data has been collected in recent decades, providing crucial information
186 pertaining to the existence of cold-trapped volatiles on the Moon. In the present paper, we collected a
187 number of global data products that were gathered into a Geographic Information System (GIS), using
188 ESRI ArcGIS software, for combined analyses.

189 These datasets include:

- 190 • Lunar Reconnaissance Orbiter Camera (LROC) data; especially the Wide Angle
191 Camera (WAC) global mosaic at 100m/pixel, and the Narrow Angle Camera (NAC) polar
192 mosaics at ~1 m/pixel (Robinson et al., 2010),
- 193 • LOLA digital elevation models available at various spatial resolutions (from 10
194 m/pixel to 120 m/pixel) and derived slope maps (Smith et al., 2017),
- 195 • LOLA-based Sun and Earth visibility obtained from time averaging of computational
196 modeling results performed every hour over ~18.6 years, and available at a resolution of 240
197 m/pixel (Mazarico et al., 2011). The average visibility is a fraction of time, equal to 0 when
198 the Sun / Earth is not visible, and 1, when any part of it is. Illumination values used in this
199 study indicate the fraction of time the Sun is visible from a given location.
- 200 • LOLA-based PSRs maps (Mazarico et al., 2011),
- 201 • LOLA albedo map at 1064 nm, at 1 km /pixel (Lucey et al., 2014; Lemelin et al.,
202 2016) and anomalously bright pixels map (Fisher et al., 2017),
- 203 • Diviner Lunar Radiometer Experiment average, minimum, and maximum bolometric
204 brightness temperature maps, as well as predicted ice depth stability at 240 m/pixel (Paige et
205 al., 2010; Williams et al., 2017),

- 206 • LPNS Hydrogen abundance maps at ~15 km / pixel (Elphic et al., 2007, Feldman et
207 al., 2001),
- 208 • LEND WEH map at ~ 2 km/ pixel (Mitrofanov et al., 2012a),
- 209 • LAMP UV and off/on band albedo ratio at 240 m/pixel (Gladstone et al., 2012; Hayne
210 et al., 2015),
- 211 • Mini Synthetic Aperture Radar (mini-SAR) Circular Polarization Ratio (CPR) map at
212 ~75 m/pixel (Spudis et al., 2009, 2010a, 2016),
- 213 • Miniature radio frequency (Mini-RF) Circular Polarization Ratio (CPR) map from Spudis et
214 al., (2013),
- 215 • USGS geological map L-1162 (Fortezzo et al., 2013, renovation of the Wilhelms
216 (1979) map),
- 217 • Clementine UVVIS color ratio mineral map (e.g., Lucey et al., 2000; Heather and
218 Dunkin, 2002), used at latitudes <80°. This RGB composite uses the 750/415nm ratio for the
219 red-channel brightness, the 415/750nm ratio for the blue channel, and the 750/1000nm ratio
220 for the green channel. Color ratios allow identifying variations in mineralogical composition
221 and/or terrain maturity.
- 222 • The Robbins et al. (2018) impact crater database.

223 All data were downloaded from the Planetary Data System or instruments' websites and added to
224 ArcGIS in a polar stereographic projection.

225

226 **4. A global survey of potential ROIs in the vicinity of the South Pole**

227 As stated above, different datasets indicative of the presence of water ice do not correlate perfectly in
228 terms of spatial distribution (Figure 2a, 2b). We identified 11 broad ROIs for future investigations by
229 combining these datasets, using the following criteria:

- 230 - Diviner average temperature < 110K (e.g., water ice is currently stable at the surface)

- 231 - Slope < 20° (Safe for landing and roving)
- 232 - Enhanced H signatures (> 100 ppm by weight, derived from LPNS data) (Ice should be
- 233 present close to the surface).

234 These 11 ROIs include a broad region around the South Pole (comprising Shackleton, De Gerlache,
235 Shoemaker, Faustini, Haworth, Nobile, Sverdrup craters) as well as smaller areas around Cabeus,
236 Amundsen northern half, Amundsen C, Idel'son, Wiechert E, Wiechert J, and Ibn Bajja craters (see
237 green circles on Figure 2b,c). These regions show evidence for surface water ice based on either
238 LAMP, LOLA or M3 datasets (e.g., Li et al., 2018; Figure 2). Eight of these ROIs are located on the
239 lunar nearside, and they are all located within the SPA basin. Thus, all the proposed ROIs offer the
240 possibility to study both volatiles and SPA geology (see section 6.2). In addition, these ROIs cover
241 various geological units, from pre-Nectarian (>3.9 Ga) to Erastosthenian in age (from 3.2 to 1.1 Ga,
242 De Gerlache, Wiechert J. for instance) and include one complex crater central peak (Amundsen),
243 which might have excavated material from depths down to 16 km (using the depth of melting
244 equation of Cintala and Grieve, 1998, in which the maximum depth of melting corresponds to the
245 minimum depth of origin of central peak material). Three of the proposed ROIs encompass
246 previously proposed sites and cover a wider area (Figure 2c), as we allowed lower hydrogen
247 abundance values than Lemelin et al. (2014) and LEAG VSAT (2015). Eight of the proposed ROIs
248 are new and rely on the availability of data analyses published since the previous ROI definitions
249 such as those based on LOLA (Fisher et al., 2017), LAMP (Hayne et al., 2015) and M3 (Li et al.,
250 2018) reflectance. ROI are not prioritized in this study, as the final choice will be strongly mission
251 dependent. Not all of the proposed ROIs offer good Sun or Earth visibility; as illumination is
252 expected to be a limiting factor for any landing site at the South Pole, this aspect will be considered
253 in the mission-specific case studies discussed below. Illumination is a key power source for most
254 proposed missions, but, as shown in Figure 1, it is anti-correlated with the average surface
255 temperature measured by Diviner. All areas of average illumination >25% around the South Pole are
256 locations where water ice is not expected to be stable at the surface according to Diviner thermal
257 models (Paige et al., 2010). Water ice is however predicted to be stable near the surface (<1 m depth)

258 at some of these locations, especially those surrounding massive PSRs (Paige et al., 2010, Figure 1).
259 Restricted areas of average illumination > 80% were identified (Mazarico et al., 2011), however they
260 should not bear water ice within the first meter of the surface (with the exception of a few pixels) and
261 are poor candidates for volatile investigations (Figure S1, S2).

262

263 **5. Selected case studies**

264 Eleven broad ROIs, which appear suitable for landing and science investigations of polar volatiles,
265 were identified in the previous section. However, identifying specific landing sites for individual
266 missions is critically dependent on the mission's goals and capabilities. We present hereafter some
267 examples of landing site analysis for mission scenarios currently under consideration. It should be
268 noted however that the findings are relevant to a broad array of mission scenarios, including human
269 missions to the lunar polar regions, for which constraints related to the environment and driving
270 objectives are likely to be comparable to robotic missions. All the polar landing sites that will be
271 proposed hereafter encompass the eleven broad ROI from this study (Figure 2c).

272 **5.1 The Luna-25 mission**

273 Luna-Glob, or Luna-25, is an upcoming Russian lander mission, which aims to study the composition
274 and physical properties of the regolith and surface volatiles in the vicinity of the lunar South Pole (e.g.,
275 Mitrofanov et al., 2012b). The Luna-25 lander will be equipped with a suite of instruments for *in situ*
276 analyses, including a neutron and gamma-ray spectrometer, a laser mass spectrometer, an IR
277 spectrometer, and several TV cameras (<http://www.iki.rssi.ru/eng/moon.htm>). Due to engineering
278 constraints, it was previously formulated that potential landing sites for Luna-25 must meet the
279 following criteria (Ivanov et al., 2015, 2017; Mitrofanov et al., 2016):

- 280 ▪ The latitude and longitude of the landing site must be between 65-85°S and 0-60°E
281 (Magenta outline on figure 1);
- 282 ▪ The landing ellipse dimensions must be 15 km ×30 km (elongated in longitudinal

- 283 direction);
- 284 ▪ Surface slopes within the landing ellipse must not be greater than 7° on a 2.5 m scale;
 - 285 ▪ The mean illumination within the landing area must be maximal;
 - 286 ▪ Earth visibility (for radio communication) within the landing area must be maximal;
 - 287 ▪ The hydrogen abundance as estimated from orbit must be maximal.

288

289 Constraints on illumination exclude higher latitude terrains and PSRs. Twelve landing ellipses located
290 between latitudes $67\text{-}74^\circ\text{S}$ have been proposed previously, using LEND data to estimate the H
291 abundance from orbit (Mitrofanov et al., 2016). Ellipse 11 on the floor of Boguslawski Crater was
292 initially selected as the most appropriate landing site candidate (e.g., Ivanov et al., 2015) but was later
293 discarded as it did not appear to present the best characteristics in terms of Earth and Sun visibility.

294 We carried out a new study of possible landing ellipses using the previously listed constraints
295 translated into our GIS. To build on previous work by Mitrofanov et al., (2016), we used both LPNS
296 and LEND H abundance estimates and favored ellipses, which showed enhanced values in both
297 datasets. By eliminating all areas with a slope $> 7^\circ$ and illumination $< 40\%$ (blackened on Figure 3b),
298 the same twelve ellipses initially identified, together with six additional candidate ellipses (labeled
299 from 13-18), can be outlined in the remaining, H-rich terrains (Figure 3a,b,c; Flahaut et al., 2016c).

300 Zonal statistics were then performed to compute mean values and standard deviations for the
301 elevation, slope, illumination, Earth visibility, H abundance, minimum, maximum and average
302 temperature, composition and age of each of the 18 proposed ellipses (Table 1, Table S1). There are
303 discrepancies between the H abundance estimates from the LPNS and LEND but some ellipses (e.g.,
304 1, 16) have high H abundance values according to data from both instruments. All the ellipses fall
305 within the same average temperature range as estimated from the Diviner bolometric temperatures
306 polar maps. Terrains within the landing ellipses appear rather homogeneous despite various ages (from
307 Imbrian to pre-Nectarian), and appear to be composed of anorthositic material according to the
308 Clementine false color RGB maps (e.g., Heather and Dunkin, 2002).

309 Ellipses 1, 6, 13 and 16 appear to have more desirable average values than other ellipses according to
310 the computed statistics. Ellipse 1, which presents slightly better illumination conditions (47%), is
311 considered a high priority site and has been studied at higher resolution by Ivanov et al. (2017)
312 together with ellipses 4 and 6. All of the ellipses 1, 6, 13, and 16 are likely to be dominated by SPA
313 basin ejecta, with local contributions from large, ancient craters such as Manzinus and Schomberger in
314 ellipse 1, and Boguslawsky and Boussingault in ellipses 6, 13 and 16 (Ivanov et al., 2017; Figure 3c).
315 However, as noted by Ivanov et al., (2017), materials ejected by Boguslawsky and Boussingault from
316 the lower portions of the SPA ejecta blanket form a smooth, hilly unit in ellipses 6, 13 and 16 that
317 appear safer for landing than the flat plains of ellipse 1, as it is less populated by steep-walled craters.

318 **5.2 The Luna-27 mission**

319 The Russian led Luna-Resurs, or Luna-27, solar-powered mission will be tasked to detect and
320 characterize lunar polar volatiles, including water ice, near the South Pole (e.g., Mitrofanov et al.,
321 2012b). Luna-27 is planned as the first step towards a future automated Russian polar sample return
322 mission (<http://www.iki.rssi.ru/eng/moon.htm>) and consists in a lander initially aimed at landing at
323 latitudes $>80^\circ$.

324 Official requirements for landing site selection have not been released yet, but from the mission's
325 objective and design, and the previous Luna missions, we infer the following constraints for the
326 purposes of this analysis:

- 327 ▪ Surface slopes at the landing site must not exceed 7° on a 2.5 m scale (or at the best
328 available scale);
- 329 ▪ The mean illumination within the landing area must be maximal;
- 330 ▪ The Earth visibility (for radio communication) within the landing area must be
331 maximal;
- 332 ▪ The hydrogen abundance as estimated from orbit must be maximal;
- 333 ▪ The surface temperature must be sufficiently low to allow for the presence of water ice
334 at or near the surface.

335 Considering the previous constraints, all areas with average surface temperature > 110 K or surface

336 slope $>7^\circ$ at 20 m (the best LOLA DEM available for latitudes $\geq 80^\circ$) were discarded. By arbitrarily
337 requiring the thresholds for the illumination fraction to be $>25\%$ and those for H abundances to be
338 >100 ppm, only 14 candidate landing sites are retained (Table 2, Figure 4a). Zonal statistics were then
339 performed to compute mean values and standard deviations for the extent, slope, illumination, Earth
340 visibility, H abundance, average temperature and surface age (Table 2, Table S2). Five of the proposed
341 sites (labeled 9, 11, 12, 13, 14) are centered on the farside and offer less than 30% Earth visibility,
342 implying that the mission would have to be assisted for operations via a relay orbiter (Figure 4b, Table
343 2). Assuming a landing ellipse size that is at least $30 \text{ km} \times 15 \text{ km}$ in size (based on the Luna-Glob
344 ellipse size), only three broad landing areas can be targeted near the South Pole: the plains of Ibn Bajja
345 (site 6 of Figure 4), the southern part of Amundsen crater (site 1, Figure 4), and the farside location
346 south of Wiechert J. crater (site 14, Figure 4). Those three areas present low slopes over areas between
347 920 and 2150 km^2 . Diviner average surface temperature varies between 37 and 140 K spatially,
348 suggesting that polar ice might not be ubiquitously present at the surface within these areas, but could
349 be present at the subsurface. However, numerous colder areas and small scale PSRs are present.
350 Among the three areas of larger extent, the plains south and west of the 12 km diameter Ibn Bajja
351 crater offer the best compromise between all criteria with an average illumination fraction of 27% ,
352 average Earth visibility of 37% and hydrogen abundance of ~ 110 ppm with LPNS and $0.12 \text{ wt}\%$
353 WEH with LEND. The highest H abundance from both LPNS and LEND data is expected at site 2
354 (Shoemaker-Faustini ridge), but illumination (25% on average) and slope (6.75° on average) are less
355 optimal and the illuminated area is more restricted in extent ($<200 \text{ km}^2$) (Table 2). All 14 proposed
356 sites present a variety of additional geologic features of interest, such as the possibility to analyze SPA
357 ejecta in ancient pre-Nectarian units or to sample relatively young Upper Imbrian and Erastosthenian
358 materials in the vicinity of Idel'son L (site 12), Wiechert J (site 14) or Shackleton (site 3).

359

360 **5.3 The ESA Lunar Prospecting Rover (LPR) study into a mission**

361 The LPR was an ESA study into a mission, consisting of a medium-class ($<250 \text{ kg}$) rover mission to
362 the South Pole of the Moon (e.g., Carpenter et al., 2015; Houdou et al., 2016). The LPR main

363 objective was to assess the distribution of water and other volatiles on a local scale during a 2-year
364 mission (2022-2024). The rover model payload included a panoramic multispectral camera, a ground
365 penetrating radar, a set of gamma-ray, neutron and IR spectrometers as well as a drill and a
366 miniaturized chemical laboratory (PROSPECT). Mission requirements included a mobile range of 50
367 km, an average illumination fraction >0.25 , and Earth visibility for direct-to-Earth communication
368 (e.g., Carpenter et al., 2015).

369 Illumination conditions are found to be the main driver for the site selection here, as most areas around
370 the South Pole do not meet the average sun visibility $> 25\%$ criteria. Earth visibility, access to at least
371 two small-scale PSRs, H abundance and access to several geologic units along the possible traverse
372 distance were used as additional criteria. Two potential sites were identified and correspond to sites
373 that were also suggested for the Luna-27 mission: Site A (also listed as site 2 in Table 2 for the Luna-
374 27 mission, Figure 5), the preferred site, is a H-rich (>150 ppm), topographic high between Shoemaker
375 and Faustini craters; Site B (listed as site 6 in Table 2 for the Luna-27 mission, Figures 4, 6) is situated
376 in the Imbrian plain southwest of Ibn Bajja. In addition to fulfilling both scientific constraints and
377 mission requirements, site A is:

- 378 ▪ located at a geologic ‘triple point’ (where three different geological units meet),
- 379 ▪ straddling a boundary between a high and low LEND H detection,
- 380 ▪ located within an area where various ice stability depths are predicted and Diviner
381 temperature is spatially variable.

382 The back-up site (site B) is in the plains around Ibn Bajja that appear to present good trafficability and
383 average illumination, variable ice stability depths, variable (including low) surface temperatures, and
384 access to two different geological units; however, average H abundances estimated from LPNS (From
385 95 to 127 ppm, 107 ppm on average) and LEND (From 0 to 0.23 wt%, 0.12 wt% on average) are
386 relatively lower (Flahaut et al., 2016 a,b; Figure 6).

387 Detailed potential traverses were developed at site A based on high-resolution observations and other
388 available datasets (Figures 5, 7, 8). Waypoints (WP) were defined in order to prepare for more

389 complex traverses that will take hourly Earth visibility and illumination variations into account. The
390 WP represent a nominal list of science stations where the rover would stop for sampling and
391 measurements that cannot be done while driving, and that would be necessary to fully achieve the
392 mission's science goals. The WP selection was defined in order to encompass:

- 393 ▪ The contact between the three geological units (1 WP),
- 394 ▪ At least 2 WP per geological unit,
- 395 ▪ At least 3 WP in different PSRs,
- 396 ▪ At least 2 WP in areas where the maximum T does not exceed 110K,
- 397 ▪ At least 2 WP each in areas where ice stability depth is predicted to be equal to 0,
398 between 0.01 - 0.25 m, and 0.25 - 0.5 m,
- 399 ▪ At least 1 WP in areas where ice stability depth is predicted to be between 0.5 - 1 m, >
400 1 m.

401 Two sets of way points are proposed, which would correspond, if following the shorter path (direct
402 line), to traverses of 22 (9 WP, set 1) and 25 km (10 WP, set 2) (Figure 7). It is not expected, in the
403 proposed scenario, that the rover returns to its landing site at the end of the mission. WP sets are built
404 around WP3, the geologic triple point, which is common to both traverses. The area of higher
405 illumination defined as site A is spatially limited by the deep Faustini crater PSR to the east,
406 Shoemaker crater deep PSR to the south, steep terrains to the north and less illuminated terrains to the
407 west (Figures 7, 8). Proposed traverse egress up to 15 km away from WP3 into the north and west
408 areas in WP set 1, to the west and south in set 2, to visit multiple, small-scale PSRs as well as areas
409 where water ice should crop out at the surface (Figure 5, 7, Table S3). Realistic traverses should
410 account for the varying conditions and preferred slope rather than the shortest path between WPs.
411 Accessibility maps for the years 2022-2024 were derived in accompanying studies (e.g., Diedrich et
412 al., 2016; Ferri et al., 2016) to select the most appropriate route as the Earth and Sun position vary.
413 These supplementary studies showed that it is possible to connect the stations while maximizing both
414 the illumination of the site (to supply sufficient energy to the solar-powered rover) as well as good

415 communication windows with Earth (to provide robust teleoperation), but with the planned design the
416 rover would have to keep chasing the light in order to operate and survive.

417

418 **6. Discussion**

419 **6.1 Candidate landing sites for volatile investigations at high latitudes**

420 A wide range of remote sensing datasets is now available and can be explored simultaneously in multi-
421 parameter analyses to optimize the selection of landing sites for future lunar missions. Following this
422 approach, we identified eleven areally broad ROIs that appear suitable for landing and general science
423 investigations of polar volatiles, followed by more specific landing sites that meet the mission
424 requirements for Luna-25, Luna-27 and LPR missions. All of the proposed landing sites for the polar
425 missions (Luna 27 and LPR study) encompass the 11 ROI that were previously defined in this study,
426 but extent beyond the ROI previously defined by VSAT (2015) and Lemelin et al. (2014). Most of the
427 proposed landing sites are located within the ROIs of higher latitudes, in the vicinity of the South Pole.
428 These example studies indicate that several factors can limit the possible areas of exploration, such as
429 the Sun and Earth visibilities. Luna-25 candidate sites are all limited to latitudes $< 70^\circ$ on the nearside
430 in order to meet high values for both criteria, therefore limiting this mission to the investigation of
431 non-polar volatiles (see section 5.1). The same region was considered for the landing site of the Indian
432 space research organization Chandrayaan-2 lander and rover due to the same restrictions on power and
433 communication (e.g., Amitabh et al., 2018). Our study shows that, in the best-case scenarios, areas of
434 acceptable slope and surface temperatures at latitudes $> 80^\circ$ would not offer more than ~35%
435 illumination and/or 50 % Earth visibility. Such values pose challenges for long-term operations of
436 solar-powered missions. Most of the suitable sites with illumination $> 25\%$ (see section 5.2) are of
437 relatively minor spatial extent (30 to a few 100s km²) and will require precise landing and small
438 landing ellipse requirements. If we consider an ellipse size similar to that of Luna-25, only three
439 possible landing areas were identified at latitudes exceeding 80° : the plains of Ibn Bajja, the southern
440 part of Amundsen crater and the farside location south of Wiechert J crater. These landing site

441 encompasses two new ROIs defined in this study. However, surface temperature and H abundances in
442 these areas vary spatially, and water ice will likely not be present within the entire area. These broad
443 areas may therefore be better suited for a rover mission, such as the LPR mission, which can reach
444 nearby cold traps, rather than a static lander.

445 It is important to note that further reduced areas ($<1 \text{ km}^2$) of higher illumination ($>78\%$) have been
446 identified on the rims of impact craters near the South Pole (Mazarico et al., 2011, Figures S1, S2).
447 However, the most illuminated areas are presumably too hot to contain near-surface volatiles and
448 therefore less interesting for scientific investigations (Figure S2). These areas could however represent
449 interesting power stations for more complex mission scenarios, assuming that high-precision landing
450 ($< \text{a few } 100 \text{ m}$) can be achieved. Our results further demonstrate that it is virtually impossible to find
451 an area of illumination $>25\%$ where water ice should be stable at the surface according to the available
452 LOLA-based illumination and Diviner thermal models (Figure 1c, g). However, in these locations,
453 water ice and other volatiles are expected to be stable at shallow depths (from a few 10's of cm to
454 meters, Paige et al., 2010) and could be accessed with a scoop or drill system.

455 **6.2 The potential for additional science benefits**

456 Lunar polar areas remain unexplored and represent key sites to address some of the top science
457 priorities of future lunar exploration (e.g., Crawford et al., 2012; NRC, 2007). In addition to
458 investigating polar volatiles (science concept 4 of the NRC 2007 report), some of the top science
459 priorities identified by the community (NRC, 2007) can be investigated at the South Pole specifically
460 – as it lies within the SPA basin (e.g., Science concept 1,2,3,5, see Kring and Durdas, 2012; Flahaut et
461 al., 2012). SPA is indeed the largest and oldest known impact structure on the Moon, and its extent
462 suggests that it may have excavated the lunar lower crust and mantle, providing a windows into the
463 lunar interior, and access to primary products of the lunar magma ocean crystallization (NRC science
464 concepts 2 and 3). Dating SPA formation (NRC concept 1) is the top-priority of the NRC (2007)
465 report as it could help anchor the period of basin formation on the Moon, and would allow to test the
466 lunar cataclysm hypothesis, but the collected samples would have to be returned back to Earth for
467 analysis, which is not planned for Luna-25, Luna-27 and the LPR missions.

468 The area that we surveyed around the South Pole is referred to as part of SPA's "heterogeneous
469 annulus", which is defined as spatially interspersed feldspathic and (minor) mafic materials comprised
470 within the basin outer part (e.g., Moriarty and Pieters, 2018). The non-mare mafic components of this
471 heterogeneous annulus are dominated by Mg-pyroxene signature, which might be indicative of SPA
472 melt and/or lower crust/mantle components (Moriarty and Pieters, 2018). Mapping the occurrence of
473 mafic minerals in the polar regions with remote sensing VNIR spectrometers is however challenging
474 because of the low illumination, and hence the low signal-to-noise ratio of the instruments. Accessing
475 these key samples might also be difficult as they may have been brecciated and covered by subsequent
476 impact ejecta. Whereas the Malapert massifs likely represent SPA rim (and therefore, highland crust
477 covered in SPA ejecta), Shackleton crater and the South Pole might be located on an inner ring on
478 SPA, which uplifted deeper material (Spudis et al., 2008). Together with the Amundsen crater central
479 peak, which is expected to contain material from depths < 16 km, the Shackleton crater, De Gerlache
480 crater, and their surroundings represent promising sites for SPA investigations near the South Pole.

481 The detailed geological record preserved in the near sub-surface at various candidate landing sites is
482 expected to vary. In addition to ancient SPA - derived material, dating Erastosthenian samples from
483 young polar craters such as Wiechert J., or well-defined units like unit Nc at site 2 (Nc is a Nectarian
484 unit that is well-bracketed in terms of stratigraphy: it is stratigraphically younger than Nectaris basin
485 but older than Imbrium basin) would be of great additional science benefit as it would enable the
486 establishment of a more precise lunar chronology. Measuring volatile elements in relatively young, or
487 only recently exposed materials could also help determine the relative contribution of indigenous and
488 exogenous volatiles (Füri et al., 2017, 2019). More work is required to define the geologic contexts,
489 and likely sub-surface environments, of all potential south polar landing sites as part of a detailed site
490 selection process. Still, additional geologic investigations of various types appear to be possible at
491 many sites.

492 **6.3 Implications for future missions**

493 Existing datasets suggest that there are no flat areas > 1 km² with illumination ≥ 50% at latitudes >
494 80°. This will impact the design and/or duration of future polar missions. Only three elevated locations

495 around Nobile crater show ~50% average illumination over a 1 km radius circle, but these areas are
496 steep and likely too warm for water ice to be present at or near the surface (Figures S1, S2). Due to
497 the rough topography of the South Pole, Earth visibility is also limited and does not reach 100% at
498 latitudes $> 86^\circ$, even on the nearside, which implies that future missions to the pole will either require
499 more autonomy or mandatory “naps”.

500 Areas of more limited illumination ($<35\%$) were identified in our study (Table 2), but targeting these
501 areas will require precise landing (as they are limited in extent, and generally $<200\text{ km}^2$) and/or access
502 to the shallow subsurface for volatile sampling using drills (as their surface temperature might be too
503 elevated for water ice to outcrop).

504 Without nuclear power, it is virtually impossible for a lander mission to directly investigate cold-trap
505 PSRs where water ice is expected to be stable at the surface, but it might be possible to land in a
506 partially illuminated/ partially shadowed crater such as Amundsen, and investigate the colder areas
507 with a rover, as suggested by Lemelin et al. (2014). However, rover missions at the pole will be
508 challenged by the rough topography at most locations, and the necessity to constantly track the light, if
509 solar-powered. Rechargeable hoppers are being considered for the Chinese polar exploration program
510 and might represent a tempting alternative to a purely static or mobile mission (e.g., Xu et al., 2019).

511 Current understanding of the spatial variation of volatile abundances at the scale of landers is a major
512 uncertainty and is a strong limitation for the use of static landers, as they could land on a volatile-free
513 area within a broader H-rich region. Nonetheless, missions to the lunar poles are key for ground-
514 truthing the recent detections and predictions of hydrogen enrichments, and to answer a number of
515 fundamental strategic knowledge gaps, such as the nature and distribution of polar volatiles, but also
516 the physical and thermal properties of the polar soil and regolith (NRC, 2007; ESA, 2019). Robotic
517 precursor missions such as those described in this study will be key to pave the way towards a
518 potential lunar base, or renewed manned exploration, which are both envisioned at the South Pole in
519 the next decade.

520 **7. Conclusions**

521 We identified eleven general regions of interest near the South Pole that would allow conducting
522 volatiles and geologic investigations. These regions have enhanced hydrogen abundances ($H > 100$
523 ppm) and temperature regimes that allow water ice to be stable at or near the surface (Diviner average
524 annual temperature < 110 K). Compelling evidence for water ice at or near the surface has been
525 reported in these ROIs by various orbital instruments (e.g., Hayne et al., 2015; Fisher et al., 2017; Li
526 and al., 2018). These ROIs include a broad area (> 200 km \times 200 km) around the lunar South Pole,
527 together with smaller regions near Cabeus, Amundsen, Ibn Bajja, Wiechert J and Idel'son craters.
528 Three of these ROIs were also previously identified by Lemelin et al. (2014) and LEAG volatile-
529 specific action team (2015) (the area near the South Pole, Amundsen and Cabeus craters) and eight are
530 new, based on our revised set of constraints and the availability of recent data analyses conducted
531 using LAMP, LOLA and M3 data. These ROIs may be key targets for future polar missions. The rich
532 science potential of these ROIs is increased by the possibility to sample South Pole Aitken basin
533 heterogeneous annulus (which may contain excavated lunar mantle material), and to date several key
534 events spanning most of the Moon's history through sample return missions.

535 Selecting more specific landing sites is highly mission dependent, and strongly limited by Earth and
536 Sun visibility in the case of solar powered-missions and /or missions without relay orbiters. Indeed, we
537 performed a detailed landing site analysis for missions with characteristics approximating those of
538 Luna-25, Luna-27 and LPR missions and obtained different results. We found that most potentially
539 volatile-bearing outcrops are not accessible to these missions because of the low average illumination
540 at the volatile-rich locations (e.g., PSRs); however, if not cropping out at the surface, water ice should
541 be present within the first meter of the surface at the sites proposed for Luna-27 and LPR like
542 missions. These sites include the ridge between Faustini and Shoemaker craters (labelled as site A or
543 site 2 in our studies), where expected H abundances are > 150 ppm, average illumination $\sim 26\%$,
544 average Earth visibility $\sim 38\%$, average surface temperature ~ 92 K (but highly variable) and average
545 slope $< 7^\circ$. We propose possible waypoints for a rover traverse at this site, and show that access to
546 small-scale PSRs within areas of enhanced illumination is possible with mobility.

547 Site A is however of limited extent, implying that precise landing will be required to investigate this
548 area. The plains of Ibn Bajja, presented as site B or site 6, are more extensive in area, but they are
549 characterized by highly variable and, on average, lower surface temperatures and H abundances,
550 suggesting that this area is not well-suited for static lander missions. The present study shows that
551 there is no single or simple scenario for *in situ* analyses and sampling of lunar polar volatiles with
552 solar-powered missions, and that trade-off in mission design and scenarios will have to be considered.
553 The use of relay orbiters may benefit future missions by extending the possibility of landing sites to
554 farside locations.

555 **8. Acknowledgments**

556 The authors wish to thank Erwan Mazarico for kindly sharing his data, as well as the editor and
557 anonymous reviewers for helpful comments. The authors are also grateful to ESA and the ESA topical
558 team on the exploitation of local planetary material for insightful discussions. This study is supported
559 by the CNES “Appel à Projets de Recherche” Luna attributed to J. Flahaut. M. Anand acknowledges
560 support from UKSA and STFC grants (#ST/P000657/1 and # ST/R001391/1, resp.). This is CRPG
561 contribution N°2718.

562 **9. References**

- 563 Amitabh, S., Srinivasan, T. P., and Suresh, K. 2018, Potential Landing Sites for Chandrayaan-2
564 Lander in Southern Hemisphere of Moon. In Lunar and Planetary Science Conference (Vol. 49, p.
565 2083).
566
- 567 Anand, M., Tartèse, R., & Barnes, J. J., 2014. Understanding the origin and evolution of water in the
568 Moon through lunar sample studies. *Phil. Trans. R. Soc. A*, 372(2024), 20130254.
569
- 570 Anand, M., Crawford, I. A., Balat-Pichelin, M., Abanades, S., van Westrenen, W., Péraudeau, G.,
571 Jaumann, R., Seboldt, W., 2012. A brief review of chemical and mineralogical resources on the Moon
572 and likely initial *in situ* resource utilization (ISRU) applications. *Planet Space Sci* 74 (1), 42-48.
573
- 574 Anand, M., 2010. Lunar Water: A Brief Review, *Earth Moon Planets* 107, 65-73.
575
- 576 Arnold, J.R., 1979. Ice in the lunar polar regions. *J. Geophys. Res.* 84, 5659–5668.
577

578 Bussey, D.B.J., McGovern, J.A., Spudis, P.D., Neish, C.D., Noda, H., Ishihara, Y., Sørensen, S.-A.,
579 2010. Illumination conditions of the South Pole of the Moon derived using Kaguya topography.
580 *Icarus*. doi:10.1016/j.icarus.2010.03.028.
581

582 Bussey, D.B.J., Lucey, P.G., Steutel, D., Robinson, M.S., Spudis, P.D., Edwards, K.D., 2003.
583 Permanent shadow in simple craters near the lunar poles. *Geophys. Res. Lett.* 30, 1278.
584 doi:10.1029/2002GL016180.
585

586 Bussey, D.B.J., Spudis, P.D., Robinson, M.S., 1999. Illumination conditions at the lunar South Pole.
587 *Geophys. Res. Lett.* 9, 1187–1190.
588

589 Carpenter, J. D., Fisackerly, R., Aziz, S., & Houdou, B., 2015. Exploring Cold Trapped Volatiles from
590 Stationary Landers and Mobile Rovers: ESA Activities for Resource Prospecting at the Poles. In
591 Annual Meeting of the Lunar Exploration Analysis Group (Vol. 1863, p. 2027).
592

593 Cintala, M. J., & Grieve, R. A., 1998. Scaling impact melting and crater dimensions: Implications for
594 the lunar cratering record. *Meteoritics & Planetary Science*, 33(4), 889-912.
595

596 Colaprete, A. et al., 2010. Detection of water within the LCROSS ejecta plume. *Science* 330, 463–
597 468. doi:10.1126/science.1186986.
598

599 Crawford, I. A., Anand, M., Cockell, C. S., Falcke, H., Green, D. A., Jaumann, R., & Wieczorek, M.
600 A., 2012. Back to the Moon: the scientific rationale for resuming lunar surface exploration. *Planetary
601 and Space Science*, 74(1), 3-14.
602

603 De Rosa, D., Bussey, B., Cahill, J.T., Lutz, T., Crawford, I.A., Hackwill, T., van Gasselt, S., Neukum,
604 G., Witte, L., McGovern, A., Grindrod, P.M., Carpenter, J.D., 2012. Characterisation of potential
605 landing sites for the European Space Agency's Lunar Lander project. *Planet. Space Sci.* 74, 224–246.
606

607 Diedrich, T. et al., 2016. Prospecting and Returning Lunar Surface Samples with Volatiles, 4th
608 European Lunar Symposium, abstract #031.
609

610 Elphic, R. C., Eke, V. R., Teodoro, L. F. A., Lawrence, D. J., & Bussey, D. B. J., 2007. Models of the
611 distribution and abundance of hydrogen at the lunar South Pole. *Geophysical Research Letters*, 34(13).
612

613 ESA, 2019. ESA strategy for Science at the Moon, available at ESA
614 (<http://exploration.esa.int/jump.cfm?oid=61371>).
615

616 ESA TT ELPM (Topical Team on the Exploitation of Local Planetary Material), 2015. A ‘European
617 response’ to the recent Lunar Exploration and Analysis Group (LEAG) Volatiles Special Action Team
618 (VSAT) report on lunar volatiles, available at ISECG.
619

620 Feldman, W.C., Maurice, S., Lawrence, D.J., Little, R.C., Lawson, S.L., Gasnault, O., Wiens, R.C.,
621 Barraclough, B.L., Elphic, R.C., Prettyman, T.H., Steinberg, J.T., Binder, A.B., 2001. Evidence for
622 water ice near the lunar poles. *J. Geophys. Res.* 106, 23231–23252.
623

624 Ferri A. et al., 2016. Lunar Volatile Prospector Mission. 4th European Lunar Symposium, abstract
625 #079.

626
627 Fisher, E. A., P. G. Lucey, M. Lemelin, B. T. Greenhagen, M. A. Siegler, E. Mazarico, O. Aharonson,
628 J.-P. Williams, P. O. Hayne, G. A. Neumann, D. A. Paige, D. E. Smith, and M. T. Zuber, 2017.
629 Evidence for surface water ice in the lunar polar regions using reflectance measurements from the
630 Lunar Orbiter Laser Altimeter and temperature measurements from the Diviner Lunar Radiometer
631 Experiment, *Icarus*, 292, 74–85.
632
633 Flahaut J. et al., 2016a. Regions of Interest for Lunar volatiles investigations : a european perspective.
634 ISECG Lunar Polar Volatiles Virtual Workshop #2, hosted by the NASA SSERVI.
635
636 Flahaut, J. et al., 2016b. Candidate landing sites near the lunar poles : a European perspective. 4th
637 European Lunar Symposium, abstract #004.
638
639 Flahaut J. et al., 2016c. Candidate landing sites for the Luna-Glob mission, 7ms3 symposium, abstract
640 # 7MS3-MN-10.
641
642 Flahaut, J., Blanchette-Guertin, J. F., Jilly, C., Sharma, P., Souchon, A., Van Westrenen, W., & Kring,
643 D. A., 2012. Identification and characterization of science-rich landing sites for lunar lander missions
644 using integrated remote sensing observations. *Advances in Space Research*, 50(12), 1647-1665.
645
646 Fortezzo, C. M., & Hare, T. M. 2013. Completed digital renovation of the 1: 5,000,000 lunar geologic
647 map series. In *Lunar and Planetary Science Conference (Vol. 44, p. 2114)*.
648
649 Füri, E., , L. Zimmermann, E. Deloule, and A.E. Saal, 2019. The H-Noble Gas Signature of Single
650 Apollo Volcanic Glass Beads. In *Lunar and Planetary Science Conference (Vol. 50, abstract #1778)*.
651
652 Füri, E., Deloule, E., & Trappitsch, R., 2017. The production rate of cosmogenic deuterium at the
653 Moon's surface. *Earth and Planetary Science Letters*, 474, 76-82.
654
655 Füri E. and Marty, B. 2015. Nitrogen isotope variations in the solar system. *Nature Geosciences*, 8,
656 515-522.
657
658 Gladstone, G.R., et al., 2012. Far-ultraviolet reflectance properties of the Moon's permanently
659 shadowed regions. *J. Geophys. Res.* 117 <http://dx.doi.org/10.1029/2011JE003913>.
660
661 Gladstone, G.R., Stern, S.A., Retherford, K.D., Black, R.K., Slater, D.C., Davis, M.W., Versteeg,
662 M.H., Persson, K.B., Parker, J.W., Kaufmann, D.E. and Egan, A.F., 2010. LAMP: the Lyman alpha
663 mapping project on NASA's Lunar reconnaissance orbiter mission. *Space Science Reviews*, 150(1-4),
664 pp.161-181.
665
666 Gläser, P., Oberst, J., Neumann, G. A., Mazarico, E., Speyerer, E. J., & Robinson, M. S., 2018.
667 Illumination conditions at the lunar poles: Implications for future exploration. *Planetary and Space*
668 *Science*, 162, 170-178.
669
670 Gläser, P., Scholten, F., De Rosa, D., Marco Figuera, R., Oberst, J., Mazarico, E., Neumann, G.A.,
671 Robinson, M.S., 2014. Illumination conditions at the lunar South Pole using high resolution Digital
672 Terrain Models from LOLA. *Icarus* 243, 78–90.
673

674 Hayne, P., O. et al., 2019. Carbon dioxide frost at the poles of the Moon: Thermal Stability and
675 observational evidence from the lunar reconnaissance orbiter. In Lunar and Planetary Science
676 Conference (Vol. 50, LPI Contrib. No. 2132).
677

678 Hayne, P.O., Hendrix, A., Sefton-Nash, E., Siegler, M.A., Lucey, P.G., Retherford, K.D., Williams,
679 J.P., Greenhagen, B.T. and Paige, D.A., 2015. Evidence for exposed water ice in the Moon's south
680 polar regions from Lunar Reconnaissance Orbiter ultraviolet albedo and temperature measurements.
681 *Icarus*, 255, pp.58-69.
682

683 Heather, D.J. and Dunkin, S.K., 2002. A stratigraphic study of southern Oceanus Procellarum using
684 Clementine multispectral data. *Planetary and Space Science*, 50(14-15), pp.1299-1309.
685

686 Houdou, B. et al., 2016. Building ESA's Lunar Exploration Mission Capabilities. 4th European Lunar
687 Symposium, abstract #051.
688

689 Ingersoll, A. P.T. Svitek B. C. Murray, 1992. Stability of polar frosts in spherical bowl-shaped craters
690 on the Moon, Mercury, and Mars. *Icarus*, 100, 40–47.
691

692 Ivanov, M. A. et al., 2017. Geological characterization of the three high-priority landing sites for the
693 Luna-Glob mission. *Planetary and Space Science*, 162, 190-206.
694

695 Ivanov, M. A. et al., 2015. Landing site selection for Luna-Glob mission in crater
696 Boguslawsky. *Planetary and Space Science*, 117, 45-63.
697

698 Kring, D. A., & Durda, D. D., 2012. A global lunar landing site study to provide the scientific context
699 for exploration of the Moon. LPI Contribution, (1694).
700

701 Lawrence, D. L., 2017. A tale of two poles: Toward understanding the presence, distribution, and
702 origin of volatiles at the polar regions of the Moon and Mercury. *J Geophys Res (Planets)* 122:21-52.
703

704 LEAG VSAT team, 2015. Volatiles Specific Action Team final report, available at
705 https://www.lpi.usra.edu/leag/reports/vsat_report_123114x.pdf.
706

707 Lemelin, M., Lucey, P. G., Neumann, G. A., Mazarico, E. M., Barker, M. K., Kakazu, A., ... & Zuber,
708 M. T., 2016. Improved calibration of reflectance data from the LRO Lunar Orbiter Laser Altimeter
709 (LOLA) and implications for space weathering. *Icarus*, 273, 315-328.
710

711 Lemelin, M., Blair, D. M., Roberts, C. E., Runyon, K. D., Nowka, D., & Kring, D. A., 2014. High-
712 priority lunar landing sites for in situ and sample return studies of polar volatiles. *Planetary and Space*
713 *Science*, 101, 149-161.
714

715 Li, S., P. G. Lucey, R. E. Milliken, P. O. Hayne, E. Fisher, J.-P. Williams, D. M. Hurley, and R. C.
716 Elphic, 2018. Direct evidence of surface exposed water ice in the lunar polar regions, *Proceedings of*
717 *the National Academy of Sciences*, 115(36), 8907–8912.
718

719 Lin, Y., van Westrenen, W., 2019. Isotopic evidence for volatile replenishment of the Moon during
720 Late Accretion. *National Science Review*, <https://doi.org/10.1093/nsr/nwz033>
721

722 Lin, Y., Tronche, E.J., Steenstra, E.S., van Westrenen, W., 2017. Evidence for an early wet Moon from
723 experimental crystallisation of the lunar magma ocean. *Nature Geoscience* 10, 14-18.
724

725 Lucey, P.G., et al., 2014. The global albedo of the Moon at 1064 nm from LOLA. *J. Geophys. Res.*
726 *Planets* 119, 1665–1679. <http://dx.doi.org/10.1002/2013JE004592>.
727

728 Lucey, P.G., Blewett, D.T., Taylor, G.J., Hawke, B.R., 2000. Imaging of lunar surface maturity. *J.*
729 *Geophys. Res.* 105.
730

731 Margot, J.L., Campbell, D.B., Jurgens, R.F., Slade, M.A., 1999. Topography of the Lunar poles from
732 radar interferometry: A survey of cold trap locations. *Science* 284,1658–1660.
733

734 Mazarico, E., Neumann, G.A., Smith, D.E., Zuber, M.T., Torrence, M.H., 2011. Illumination
735 conditions of the lunar polar regions using LOLA topography. *Icarus* 211, 1066–1081.
736

737 McGovern, J.A., Bussey, D.B., Greenhagen, B.T., Paige, D.A., Cahill, J.T.S., Spudis, P.D., 2013.
738 Mapping and characterization of non-polar permanent shadows on the lunar surface. *Icarus* 223, 566–
739 581.
740

741 Mitrofanov, I., M. Djachkova, M. Litvak, A. Sanin, 2016. The Method of Landing Sites Selection for
742 Russian Lunar Lander Missions, 18, EGU2016, abstr. 10018.
743

744 Mitrofanov, I., Litvak, M., Sanin, A., Malakhov, A., Golovin, D., Boynton, W., Droege, G., Chin, G.,
745 Evans, L., Harshman, K., Fedosov, F., Garvin, J., Kozyrev, A., McClanahan, T., Milikh, G.,
746 Mokrousov, M., Starr, R., Sagdeev, R., Shevchenko, V., Shvetsov, V., Tret'yakov, V., Trombka, J.,
747 Varenikov, A., Vostrukhin, A., 2012a. Testing polar spots of water-rich permafrost on the Moon:
748 LEND observations onboard LRO. *J. Geophys. Res. (Planets)* 117, 0.
749

750 Mitrofanov, I. G., Zelenyi, L. M., Tret'yakov, V. I., 2012b. Upgraded Program of Russian Lunar
751 Landers: Studying of Lunar Poles. LEAG meeting, abstract #3025.

752 Moriarty, D.P. and Pieters, C.M., 2018. The Character of South Pole - Aitken Basin: Patterns of
753 Surface and Subsurface Composition. *Journal of Geophysical Research: Planets*, 123(3), pp.729-747.
754

755 Noda, H. et al., 2008. Illumination conditions at the lunar polar regions by KAGUYA (SELENE) laser
756 altimeter. *Geophys. Res. Lett.* 35, 24203; doi:10.1029/2008GL035692.
757

758 Nozette, S., Spudis, P.D., Robinson, M.S., Bussey, D.B.J., Lichtenberg, C. and Bonner, R., 2001.
759 Integration of lunar polar remote - sensing data sets: Evidence for ice at the lunar South Pole. *Journal*
760 *of Geophysical Research: Planets*, 106(E10), pp.23253-23266.
761

762 Nozette, S., Lichtenberg, C.L., Spudis, P., Bonner, R., Ort, W., Malaret, E., Robinson, M., Shoemaker,
763 E.M., 1996. The Clementine bistatic radar experiment. *Science* 274, 1495–1498.
764 doi:10.1126/science.274.5292.1495.
765

766 NRC (National Research Council) 2007. *The Scientific Context for Exploration of the Moon.*
767 Washington, DC: The National Academies Press. <https://doi.org/10.17226/11954>.
768

769 Paige, D.A. et al., 2010. Diviner lunar radiometer observations of cold traps in the Moon's south polar
770 region. *Science* 330, 479–482. doi:10.1126/science.1187726.
771

772 Patterson, G.W., Stickle, A.M., Turner, F.S., Jensen, J.R., Bussey, D.B.J., Spudis, P., Espiritu, R.C.,
773 Schulze, R.C., Yocky, D.A., Wahl, D.E. and Zimmerman, M., 2017. Bistatic radar observations of the
774 Moon using Mini-RF on LRO and the Arecibo Observatory. *Icarus*, 283, pp.2-19.
775

776 Pieters, C.M., Goswami, J.N., Clark, R.N., Annadurai, M., Boardman, J., Buratti, B., Combe, J.P.,
777 Dyar, M.D., Green, R., Head, J.W. and Hibbitts, C., 2009. Character and spatial distribution of
778 OH/H₂O on the surface of the Moon seen by M3 on Chandrayaan-1. *science*, 326(5952), pp.568-572.
779

780 Robbins, S.J., 2018. A new global database of lunar impact craters >1–2 km: 1. Crater locations and
781 sizes, comparisons with published databases, and global analysis, *Journal of Geophysical Research:*
782 *Planets*, 123, <https://doi.org/10.1029/2018JE005592>.
783

784 Robinson, M. S. et al., 2010. Lunar reconnaissance orbiter camera (LROC) instrument overview.
785 *Space science reviews*, 150(1-4), 81-124.
786

787 Sanin, A. B. et al., 2016. Hydrogen distribution in the lunar polar regions. *Icarus*, 283, 20-30,
788 doi:10.1016/j.icarus.2016.06.002.
789

790 Siegler, M., Paige, D., Williams, J.P. and Bills, B., 2015. Evolution of lunar polar ice stability. *Icarus*,
791 255, pp.78-87.
792

793 Smith, D. E. et al., 2017. Summary of the results from the Lunar Orbiter Laser Altimeter after seven
794 years in lunar orbit. *Icarus*, 283, 70-91.
795

796 Speyerer, E.J., Robinson, M.S., 2013. Persistently illuminated regions at the lunar poles: Ideal sites for
797 future exploration. *Icarus* 222, 122–136.
798

799 Spudis P.D. et al., 2016. Radar Data and Lunar Polar Volatiles. ISECG Lunar Polar Volatiles Virtual
800 Workshop #1, hosted by the NASA SSERVI.
801

802 Spudis, P.D., Bussey, D.B.J., Baloga, S.M., Cahill, J.T.S., Glaze, L.S., Patterson, G.W., Raney, R.K.,
803 Thompson, T.W., Thomson, B.J., Ustinov, E.A., 2013. Evidence for water ice on the moon: results for
804 anomalous polar craters from the LRO Mini-RF imaging radar. *J. Geophys. Res. (Planets)* 118, 2016–
805 2029.
806

807 Spudis, D. B. J., B. Butler, L. Carter, M. Chakraborty, J. Gillis-Davis, J. Goswami, E. Heggy et al.,
808 2010a. Results of the mini-SAR imaging radar, Chandrayaan-1 mission to the Moon, LPSC 41st,
809 abstract #1224.
810

811 Spudis, P. D. et al., 2010b. Mini-SAR Imaging Radar and Lunar Polar Ice. In *European Planetary*
812 *Science Congress*, Vol. 5, #EPSC2010-396.
813

814 Spudis, P. D. et al., 2009. Mini-SAR: an imaging radar experiment for the Chandrayaan-1 mission to
815 the Moon. *Current Science*, 533-539.
816

817 Spudis, P.D., Bussey, B., Plescia, J., Josset, J.L. and Beauvivre, S., 2008. Geology of Shackleton
818 Crater and the south pole of the Moon. *Geophysical Research Letters*, 35(14).
819
820 Spudis, P.D., Gillis, J.J. and Reisse, R.A., 1994. Ancient multiring basins on the Moon revealed by
821 Clementine laser altimetry. *Science*, 266(5192), pp.1848-1851.
822
823 Sunshine, J. M., Farnham, T. L., Feaga, L. M., Groussin, O., Merlin, F., Milliken, R. E., & A'Hearn,
824 M. F., 2009. Temporal and spatial variability of lunar hydration as observed by the Deep Impact
825 spacecraft. *Science*, 326(5952), 565-568.
826
827 Teodoro LFA, Eke VR, Elphic RC 2010. Spatial distribution of lunar polar hydrogen deposits after
828 Kaguya (SELENE). *Geophys Res Let* 37:L12201.
829
830 Watson, K., Murray, B., Brown, H., 1961. On the possible presence of ice on the Moon. *J. Geophys.*
831 *Res.* 66, 1598–1600.
832
833 Wilhelms, D.E., Howard, K.A. and Wilshire, H.G., 1979. Geologic map of the south side of the Moon.
834 Department of the Interior, US Geological Survey.
835
836 Williams, J. P., Paige, D. A., Greenhagen, B. T., & Sefton-Nash, E., 2017. The global surface
837 temperatures of the Moon as measured by the Diviner Lunar Radiometer Experiment. *Icarus*, 283,
838 300-325.
839
840 Xu, L., Y. L. Zou and L. Qing, 2019. Overview of China's lunar exploration program and scientific
841 vision for future missions. In: *Lunar and Planetary Science Conference (Vol. 50, LPI Contrib. No.*
842 *2132)*.
843
844 Zhang, J.A., Paige, D.A., 2009. Cold-trapped organic compounds at the poles of the moon and
845 Mercury: implications for origins. *Geophys. Res. Lett.* 36 [http://dx.doi.org/ 10.1029/2009GL038614](http://dx.doi.org/10.1029/2009GL038614).
846
847 Zuber, M.T., Smith, D.E., 1997. Topography of the lunar south polar region: Implications for the size
848 and distribution of permanently shaded areas. *Geophys. Res. Lett.* 24, 2183–2186.
849

850 **10. Figure captions**

851 **Figure 1:** Maps of the lunar South Pole, from latitudes 65 to 90° S (polar stereographic projection). a)
852 LOLA DEM overlain on the LROC WAC mosaic. The blue line indicates the outline of the SPA
853 impact basin. The magenta outline indicates the region investigated for Luna-25 landing sites. Sites
854 that are recommended for the Luna-27 (black and green) and the LPR (green) case studies are also
855 shown (see next sections). b) LOLA-derived slope map at 120 m/ pixel. c) Average visibility of the
856 Sun as seen from a given point on the Moon. Visibility varies between 0, when the sun is not visible,

857 and 1, when any part of it is. Red dots indicate the highly illuminated sites discussed in Mazarico et al.
858 (2011) (Also see figure S1). d) Average visibility of Earth as seen from a given point on the Moon.
859 Visibility varies between 0, when Earth is not visible, and 1, when any part of it is. e) LPNS H
860 abundance map. Contours at 100 ppm (blue), 125 ppm (yellow) and 150 ppm (red) are indicated to
861 highlight enhanced signatures. f) LEND water-equivalent hydrogen map. Contours at 0.1 wt% (blue),
862 0.2 wt% (yellow) and 0.5wt% (red) are indicated to highlight enhanced signatures. g) Diviner average
863 temperature map. h) Excerpt of the USGS geological map L-1162. The reader is to refer to the text for
864 data resolution and sources.

865 **Figure 2:** Maps of the lunar South Pole, from latitudes 80 to 90° S (polar stereographic projection). a)
866 LAMP UV albedo anomalies, LOLA anomalously bright pixels (which might be indicative of surface
867 frost) as well as mini-SAR and mini-RF high CPR anomalies (which might be indicative of water ice
868 at shallow depths, or freshly exposed material) and M3 VNIR ice detections are overlain on the LROC
869 WAC mosaic. The blue line indicates the outline of the SPA impact basin. b) Proposed ROIs (green
870 circles) are overlain on a map where Diviner average temperature > 110K and slope values > 20° were
871 blackened. These ROIs encompass regions of enhanced H abundance, PSRs and regions with average
872 T < 54K (where CO₂ ice should be stable at the surface). c) Proposed ROIs are compared with previous
873 studies; background is a LPNS H abundance map.

874 **Figure 3:** Location of the 18 candidate ellipses within the region of interest for Luna-25 (magenta
875 outline). a) Previous proposed ellipses described in Mitrofanov et al., (2016), and additional ones from
876 this study are displayed on the LOLA topographic map. b) Comparison of the ellipses locations and
877 the LEND H-rich regions. c) Comparison of the ellipses locations and the LPNS H-rich regions. All
878 maps are overlain in transparency over the LROC WAC global mosaic and presented in polar
879 stereographic projection.

880 **Figure 4:** Location of the 14 candidate landing sites for a Luna-27 type mission aimed at investigating
881 polar volatiles at southern high latitudes (>80°). a) Proposed ROIs of relatively high illumination
882 (>25%) and elevated H (>100 ppm) are indicated (white outlines), areas of Diviner average

883 temperature $> 110\text{K}$ and /or slope values $> 7^\circ$ were blackened. The background is the average
884 visibility of the Sun map from Mazarico et al. (2011). b) Same as a), but with the background is the
885 average visibility of the Earth map from Mazarico et al. (2011). c) The proposed sites are displayed
886 over the LPNS H abundance data and compared to LAMP UV anomalies and PSRs locations (please
887 refer to the text for data sources).

888 **Figure 5:** Close-up of LPR site A, the Shoemaker-Faustini ridge. The white outlines represent the
889 areas of higher illumination, low slope and low diviner T as described in section 5.2 (Sites 2, 4, and 5
890 are shown on this close-up). The data is shown in transparency over LRO WAC + NAC polar mosaics
891 P870S0450, P870S0750, P870S1050, P880S0225, P880S0675, P880S1125, P892S0450 and
892 P892S1350. a) Illumination map, b) Slope map, c) Diviner average annual surface temperature map, d)
893 Ice stability depth map, as predicted by Diviner thermal models, e) LEND hydrogen abundance map.
894 The 150 ppm H abundance limit of LPNS is indicated as a red line as in previous figures. LAMP UV
895 albedo anomalies (which may indicate the presence of surface frost) are also represented. f) Geological
896 map (for data sources, please refer to section 2: Datasets and method).

897 **Figure 6:** Close-up of LPR site B, the Ibn Bajja plains. The white outline represents the areas of
898 higher illumination, low slope and low diviner T drawn in section 5.2. The data is shown in
899 transparency over LRO WAC + NAC polar mosaics P860S2587, P860S2812, P870S2550 and
900 P870S2850. a) Illumination map, b) Slope map, c) Diviner average annual surface temperature map, d)
901 Ice stability depth map, as predicted by Diviner thermal models, e) LEND hydrogen abundance map.
902 The 100 and 125 ppm H abundance limits of LPNS are indicated as blue and yellow lines respectively.
903 LAMP UV albedo anomalies (which may indicate the presence of surface frost) are also represented
904 and present within the area. f) Geological map (for data sources, please refer to section 2: Datasets and
905 method).

906 **Figure 7:** Examples of waypoints that could be used to establish a traverse at LPR test site A.
907 Waypoints were defined as possible ground stations where different conditions are expected and where
908 various parameters could be measured. Two sets of waypoints (green triangles and red squares)

909 starting from WP3 – the intersection of three geologic units – are shown here. The white outline
910 indicates LPR site A (Fig. 5). White circles represent a 5, 10 and 15 km buffer zone away from WP3.
911 Both traverses extend beyond the area of higher illumination towards PSRs and represent a minimum
912 path of 22 km (WP set 1) and 25 km (WP set 2) respectively.

913 **Figure 8:** 3D view of the South Pole area with WP sets 1 (red) and 2 (green). LROC WAC data at
914 100m/pixel are projected using LOLA 80 S DEM at 20 m/pixel as base height.

915

916 **Supplementary figures**

917 **Figure S1:** The 50 most illuminated locations in the vicinity of the South Pole (from Mazarico et al.,
918 2011, their table 3), which all receive > 78% illumination on average. A 1 km radius circle was drawn
919 around these areas to compute the statistics presented in Figure S2. CR = Connecting Ridge, S =
920 Shackleton, S-F = Shackleton-Faustini ridge, DG = De Gerlache, Mal. = Malapert, M-N = Malapert-
921 Nobile ridge, N1= Nobile 1, N2 = Nobile 2.

922 **Figure S2:** Terrain characteristics at high illumination sites (spatially averaged within a 1 km buffer
923 zone). Average slope, H abundance from LPNS and LEND, Diviner minimum (Tmin), maximum
924 (Tmax), and average (avgT) temperatures, Diviner thermal amplitude (Tdiff = Tmax-Tmin), and
925 average illumination (red squares) computed over a 1km radial buffer around the highest illumination
926 spots of Mazarico et al. (2011) are presented. Average illumination values over the 3.14 km² circular
927 areas are well below 60%. Average slope values are generally high (10-25°), suggesting that these
928 areas (which are mostly located on rims and ridges) are rather risky for landing. Most sites exhibit
929 Diviner average temperatures > 110K suggesting water ice is likely not present at these locations.
930 LPNS H abundances are still elevated – which is likely an artefact due to the LPNS pixel size (15 km),
931 a single LPNS pixel being much larger than the investigated areas and likely overprinting the
932 signatures of the surrounding PSRs.

933

Table 1 : Mean values of selected parameters, obtained for each of the Luna-25 18 proposed ellipses. Green and red colors highlight excellent and poor values respectively. Only ellipses 1, 2, 6, 13, and 16 fit all of the criterias listed above, the other ellipses fail at least one of those. However ellipse 2 has the worst illumination conditions and lowest H abundance, as estimated from orbit, compared to the other ones and is therefore listed as of intermediate priority. Standard deviation (STD) values are presented in table S1.

Ellipse #	Center longitude	Center latitude	Earth Visibility	Illumination fraction	H abundance from LPNS (ppm)	WEH from LEND (%)	LOLA elevation (m)	LOLA slope at 60 m (°)	Avg T from Diviner (°K)	Geol. unit	Unit description	Proposed priority ranking
1	21.21	-68.78	1.00	0.47	62	0.13	688	7.6	165	Ntp	Nectarian terra mantling and plains material	high
2	25.69	-67.38	1.00	0.43	43	0.08	-2499	6.2	162	Ip	Imbrian plains material	intermediate
3	24.61	-67.49	1.00	0.42	45	0.13	-2536	5.8	161	Ip	Imbrian plains material	low
4	11.57	-68.66	0.98	0.46	57	0.11	828	8.3	162	Ip	Imbrian plains material	low
5	23.66	-70.70	1.00	0.46	41	0.00	938	7.8	160	Ntp	Nectarian terra mantling and plains material	low
6	43.58	-69.55	1.00	0.45	78	0.12	460	9.5	161	pNbr	pre-Nectarian basin material, rugged	high
7	50.13	-72.16	0.92	0.44	69	0.19	2068	16.9	165	pNc	pre-Nectarian crater material	low
8	26.39	-73.88	0.99	0.43	37	0.08	1772	10.3	154	Isc	Imbrian secondary crater material	low
9	8.21	-71.73	1.00	0.41	64	0.00	-819	9.1	155	Esc	Erastosthenian secondary crater material	low
10	10.28	-70.15	1.00	0.41	74	0.14	119	15.5	165	Ec	Erastosthenian crater material, younger than most mare materials	low
11	43.94	-73.41	1.00	0.44	54	0.00	-872	6.4	158	Ntp	Nectarian terra mantling and plains material	low
12	26.74	-70.94	0.92	0.40	57	0.06	974	16.8	156	pNc	pre-Nectarian crater material	low

13	41.48	-69.17	0.99	0.46	66	0.06	353	9.0	163	pNb	pre-Nectarian basin materials	high
14	44.29	-67.02	0.99	0.43	42	0.11	-1959	8.0	165	pNc	pre-Nectarian crater material	low
15	31.79	-66.82	1.00	0.46	93	0.00	1542	7.9	166	pNt	pre-Nectarian terra material	intermediate
16	39.89	-68.01	0.99	0.47	84	0.10	377	9.0	159	pNb	pre-Nectarian basin materials	high
17	35.10	-69.45	0.99	0.47	74	0.00	623	9.2	160	pNb	pre-Nectarian basin materials	intermediate
18	37.33	-68.15	1.00	0.47	87	0.00	103	8.6	160	pNb	pre-Nectarian basin materials	intermediate

Table 2 : Mean values of selected parameters obtained for each of the Luna-27 14 proposed landing sites at latitudes > 80°S (see selection criteria in section 5.2). Green and red colors highlight excellent and poor values respectively. All sites have pros and cons and offer access to various geologic materials. Site 2 and 6, which have good average values for each parameter presented here, were selected for the LPR case study presented in section 5.3. Standard deviation (STD) values are presented in table S2.

site ID	Name	center lat.	center long.	area (km2)	avg Earth visibility	avg illum.	LPNS H (ppm)	LEND H (wt%)	slope at 20 m (°)	diviner avg T (K)	geol. unit	unit description
1	South Amundsen	-85.0	90.0	920	0.32	0.26	94	0.13	4.0	92	Ip (+ Nc)	Plan material, Imbrian system (+ Nectarian floor and peak of the crater)
2	Shoemaker-Faustini ridge	-87.1	65.4	191	0.38	0.26	167	0.27	6.8	92	pNbr + pNc + Nc	Basin Material, Rugged, pre-Nectarian System + Crater Material Older Than Nectaris Basin, pre-Nectarian System + Crater Material Younger Than Nectaris Basin but Older Than Imbrium Basin, Nectarian System
3	Near Shackleton	-89.5	25.5	37	0.50	0.27	143	0.25	7.1	93	pNbr	Basin Material, Rugged, pre-Nectarian System
4	Faustini ridge	-87.6	103.7	101	0.31	0.26	149	0.29	6.1	84	pNbr	Basin Material, Rugged, pre-Nectarian System
5	Near Shackleton	-88.6	101.4	83	0.39	0.24	151	0.19	7.6	91	pNbr (+Ec)	Basin Material, Rugged, pre-Nectarian System + Erastosthenian material of Shackleton
6	South / West Ibn Bajja	-86.4	-86.7	2146	0.37	0.27	107	0.12	4.8	92	Ip + pNbr	Plan material, Imbrian system + Basin Material, Rugged, pre-Nectarian System
7	South Cabeus B.	-84.0	-60.5	75	0.55	0.28	158	0.05	4.6	98	pNbr	Basin Material, Rugged, pre-Nectarian System
8	North de Gerlache	-87.9	-65.1	30	0.50	0.32	137	0.28	6.0	95	pNbr	Basin Material, Rugged, pre-Nectarian System
9	North Sverdrup	-87.4	-148.2	211	0.21	0.26	108	0.17	5.5	86	pNbr	Basin Material, Rugged, pre-Nectarian System
10	West Sverdrup	-88.0	173.2	75	0.33	0.29	136	0.23	5.9	84	pNbr	Basin Material, Rugged, pre-Nectarian System
11	South Wiechert P.	-87.2	146.7	243	0.26	0.28	131	0.23	4.5	83	Ntp	Terra-Mantling and Plains Material, Nectarian System
12	South Idel'son L.	-84.6	115.7	290	0.23	0.32	105	0.11	4.3	91	Ntp (+ Ic2)	Terra-Mantling and Plains Material, Nectarian System (+ Upper Imbrian material of Idel'son L crater)
13	West Amundsen	-85.8	112.7	188	0.23	0.37	99	0.11	4.1	99	Ntp	Terra-Mantling and Plains Material, Nectarian System
14	South Wiechert J.	-86.5	176.6	1691	0.08	0.29	99	0.19	5.0	91	Ntp (+ Ec)	Terra-Mantling and Plains Material, Nectarian System + Erastosthenian material of Wiechert J crater

Supplementary Table S1: STD values of selected parameters computed for the Luna-25 candidate ellipses and presented in Table 1.

ellipse #	Earth Visibility STD	Illumination STD	LPNS H STD	WEH from LEND STD	elev STD	slope 60 m STD	Avg T STD
1	0.007	0.017	2.019	0.008	136.889	5.986	14.672
2	0.012	0.014	5.894	0.056	57.359	6.360	12.376
3	0.005	0.012	3.253	0.009	56.937	5.283	15.281
4	0.111	0.051	0.936	0.040	114.946	6.710	8.768
5	0.023	0.027	1.932	0.017	174.568	6.292	12.861
6	0.023	0.024	8.373	0.031	274.368	5.552	11.213
7	0.144	0.034	5.241	0.018	1275.522	11.481	16.686
8	0.058	0.026	2.480	0.064	464.814	6.662	10.939
9	0.017	0.019	3.725	0.000	212.735	7.049	9.231
10	0.020	0.024	4.837	0.015	1145.140	10.595	14.356
11	0.035	0.014	0.831	0.000	87.660	5.402	10.143
12	0.165	0.062	2.640	0.053	957.978	10.145	21.220
13	0.040	0.022	3.679	0.067	339.424	5.821	15.001
14	0.056	0.023	8.370	0.046	121.185	6.855	10.464
15	0.016	0.018	0.926	0.000	238.065	5.884	13.662
16	0.041	0.025	1.332	0.027	354.281	5.454	10.390
17	0.040	0.029	1.700	0.000	222.212	6.007	13.630
18	0.029	0.026	1.168	0.000	210.333	5.850	12.824

Supplementary Table S2: STD values of selected parameters computed for the Luna-27 proposed sites and presented in Table 2.

site ID	Name	avg Earth visibility STD	avg illumination STD	LPNS H (ppm) STD	LEND H (wt%) STD	slope at 20 m (°) STD	diviner avg T (K) STD
1	South Amundsen	0.10	0.06	3.36	0.06	3.88	8.66
2	Shoemaker-Faustini ridge	0.09	0.10	3.97	0.02	4.08	15.43
3	Near Shackleton	0.04	0.09	0.00	0.00	3.88	14.52
4	Faustini ridge	0.11	0.12	0.00	0.00	3.85	18.86
5	Near Shackleton	0.17	0.12	0.06	0.02	4.82	16.14
6	South / West Ibn Bajja	0.12	0.08	8.47	0.07	4.00	12.62
7	South Cabeus B.	0.10	0.07	0.00	0.06	3.29	10.11
8	North de Gerlache	0.02	0.06	0.00	0.01	3.54	7.56
9	North Sverdrup	0.13	0.07	2.26	0.09	4.10	14.08
10	West Sverdrup	0.11	0.14	0.00	0.00	4.10	15.51
11	South Wiechert P.	0.11	0.11	1.49	0.02	3.45	13.84
12	South Idel'son L.	0.11	0.07	4.07	0.07	2.64	9.49
13	West Amundsen	0.08	0.06	1.36	0.02	2.73	7.28
14	South Wiechert J.	0.08	0.08	6.13	0.03	3.77	11.50

Supplementary Table S3: LPR proposed waypoints (WP) and their characteristics.

WP set	WP#	rationale	Geol. unit	Diviner Ice Stability Depth (ISD)	Long	lat
1	3	geologic triple point	all 3	>1 m	68.40	-86.96
1	6	T _{max} <110K	PNbr	0	65.77	-86.86
1	5	PSR	PNbr	0	66.21	-86.88
1	2	Geol unit PNc	PNc	0.38	69.34	-87.01
1	8	T _{max} <110K	Nc	0.01	69.46	-86.77
1	7	PSR	Nc	0.01	68.09	-86.77
1	1	Geol unit PNc	PNc	0.41	69.50	-87.08
1	4	1>ISD> 0.5	Nc/PNbr	0.7	68.06	-86.91
1	9	PSR, T _{max} <110K	Nc	0.01	67.25	-86.66
2	3	geologic triple point, ISD>1m	all 3	>1m	68.40	-86.96
2	8	max T<110	pNbr	0.3	64.78	-87.22
2	7	PSR	pNbr	0.01	64.08	-87.15
2	9	PSR, max T<110	pNc	0.01	66.75	-87.40
2	10	max T<110, ISD=0	pNc	0	67.31	-87.40
2	5	PSR	pNbr	0	64.40	-86.98
2	1	Geol unit Nc,	Nc	0.2	68.76	-86.85
2	2	Geol unit Nc	Nc	0.6	68.77	-86.91
2	4	1>ISD> 0.5	pNbr	0.9	67.53	-86.93
2	6	0.5>ISD>0.25	pNbr	0.3	64.37	-87.10

Figure 1

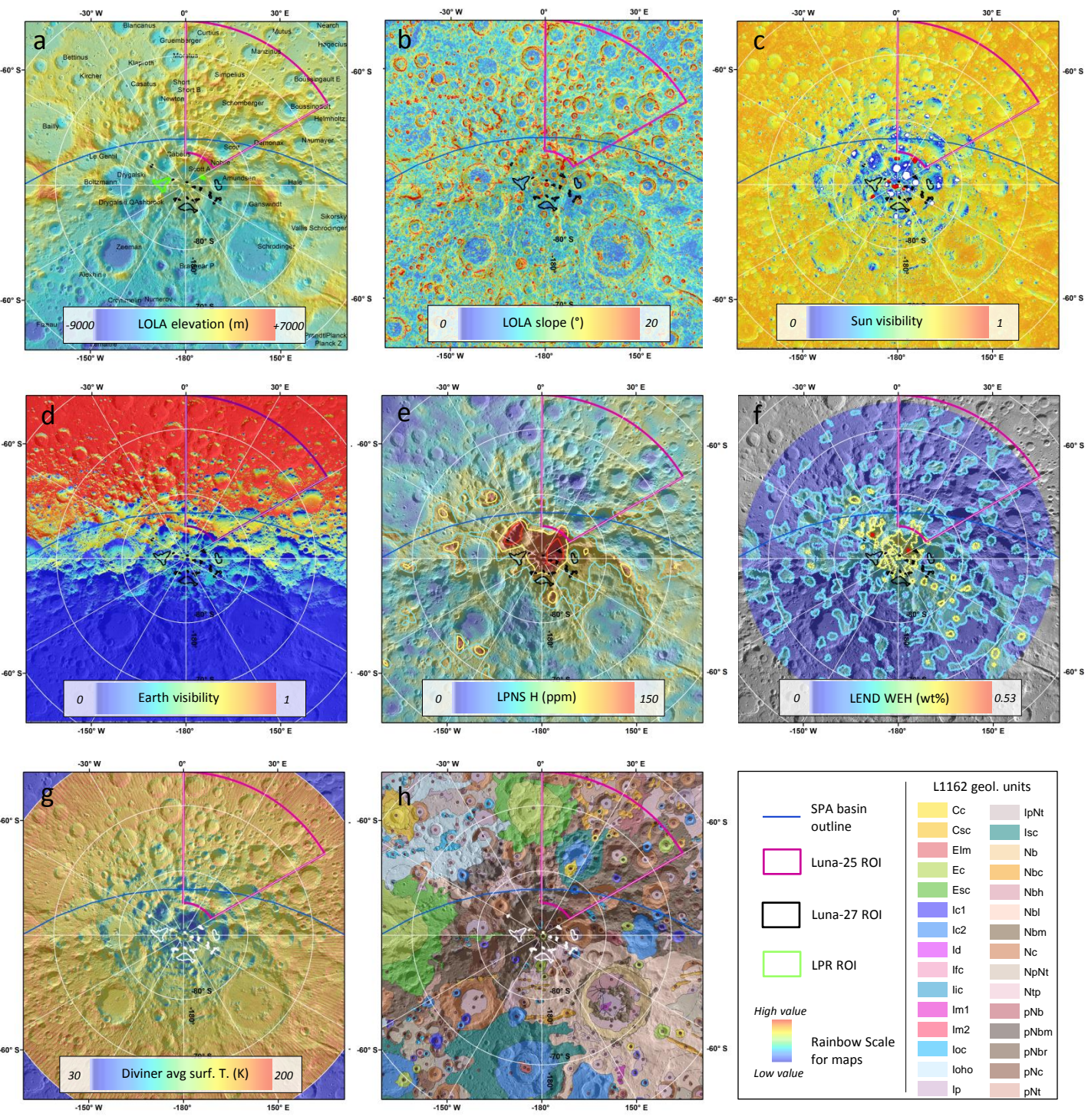
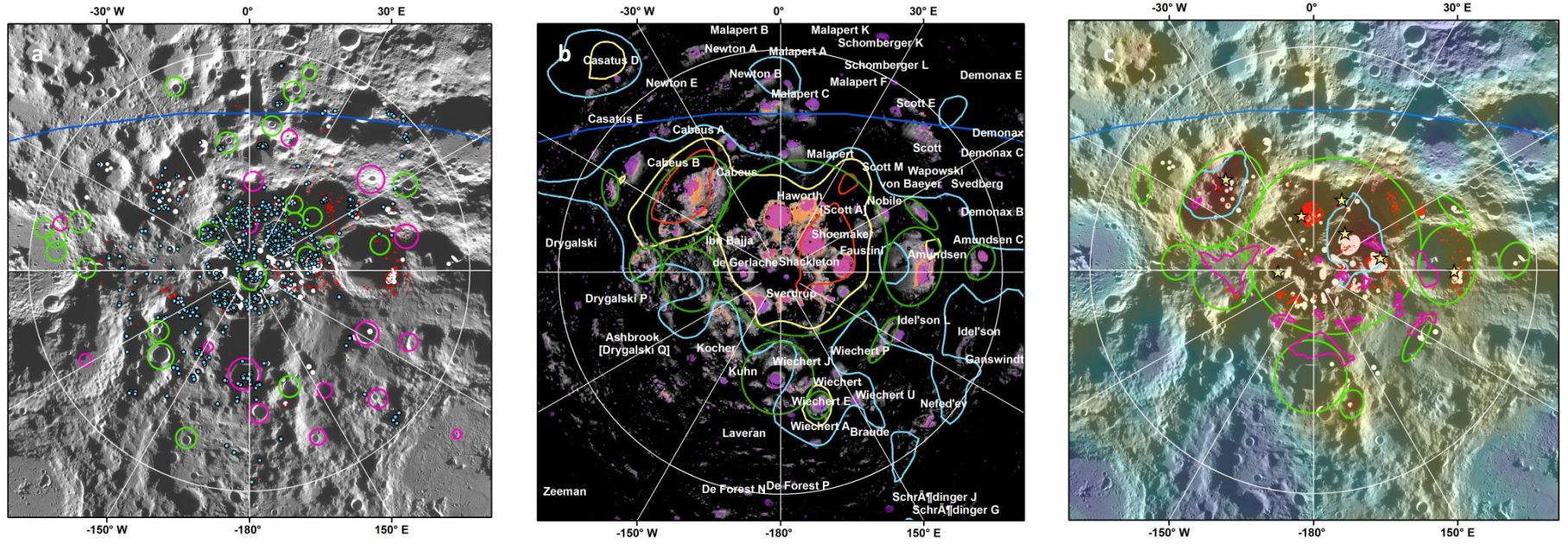


Figure 2



Mini-SAR high CPR anomaly
(Spudis et al., 2010)

Mini-RF high CPR anomaly
(Spudis et al., 2013)

LAMP UV albedo anomaly
(Hayne et al., 2015)

LOLA albedo anomaly
(Fisher et al., 2017)

UV+ VNIR spectral evidence for water ice
(Li et al., 2018)

SPA basin outline

PSRs (Mazarico et al., 2011)

Regions with avg $T < 54^{\circ}\text{K}$

Proposed ROI (this study)

110 K
30 K
Diviner avg T

LPNS H abundance contours

180 ppm

LPNS H abundance
0 ppm

Proposed ROI (this study)

Proposed sites for Luna-27 (this study)

Previous ROI from the LEAG VSAT (2015)

Previous ROI from the Lemelin et al. (2014)

Figure 3

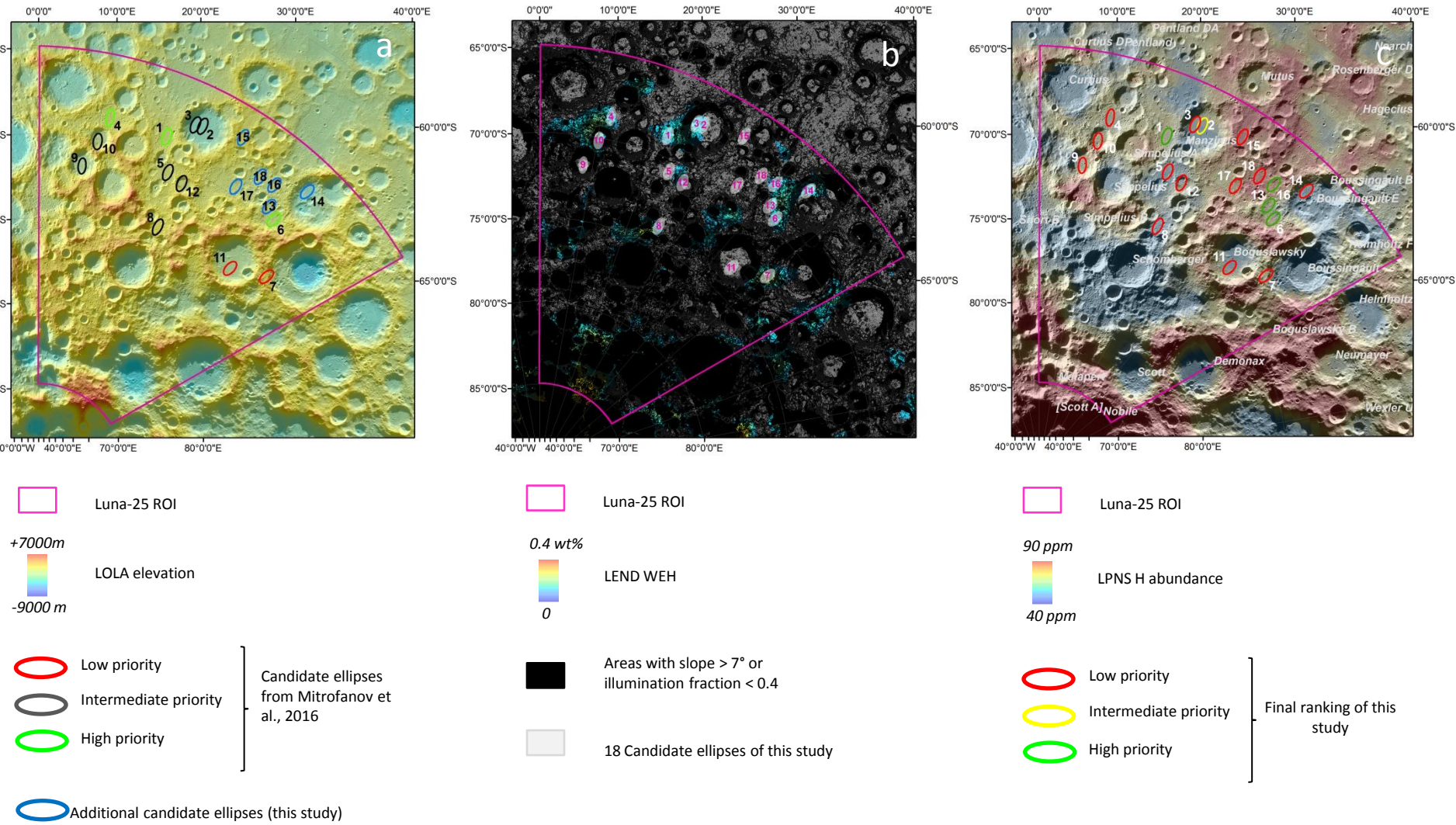


Figure 4

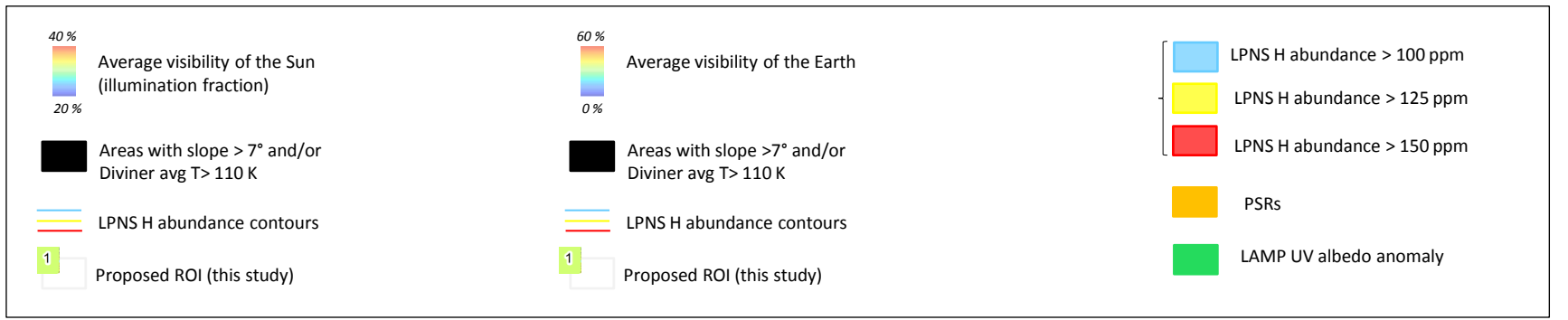
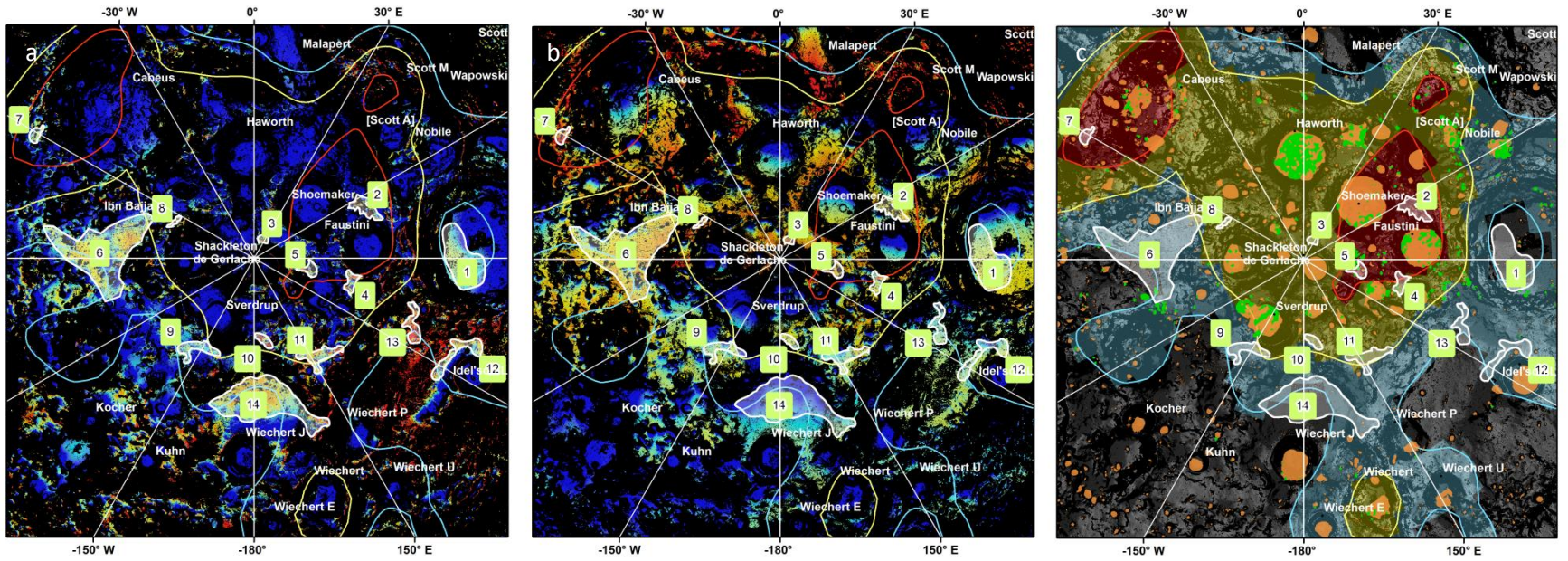


Figure 5

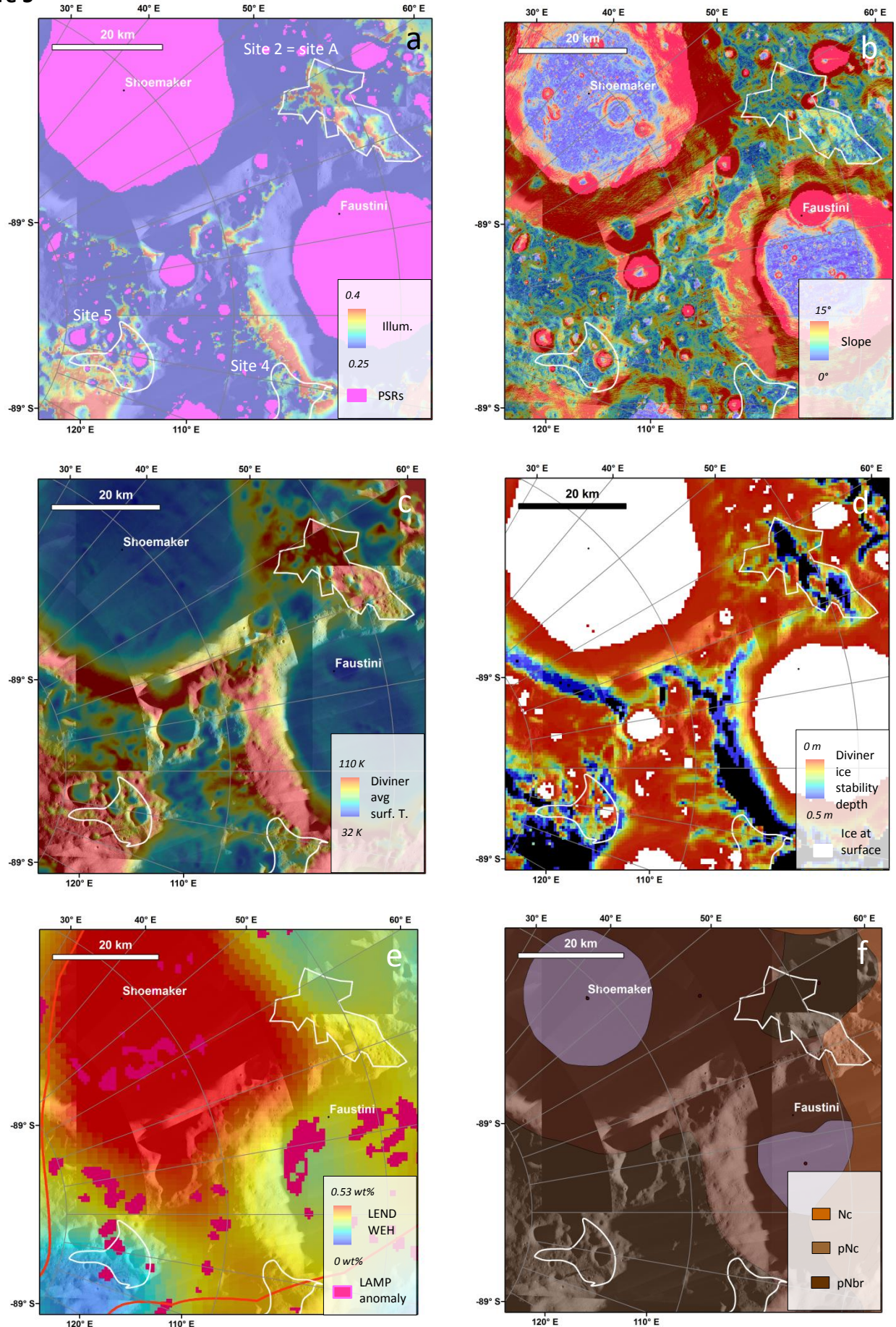


Figure 6

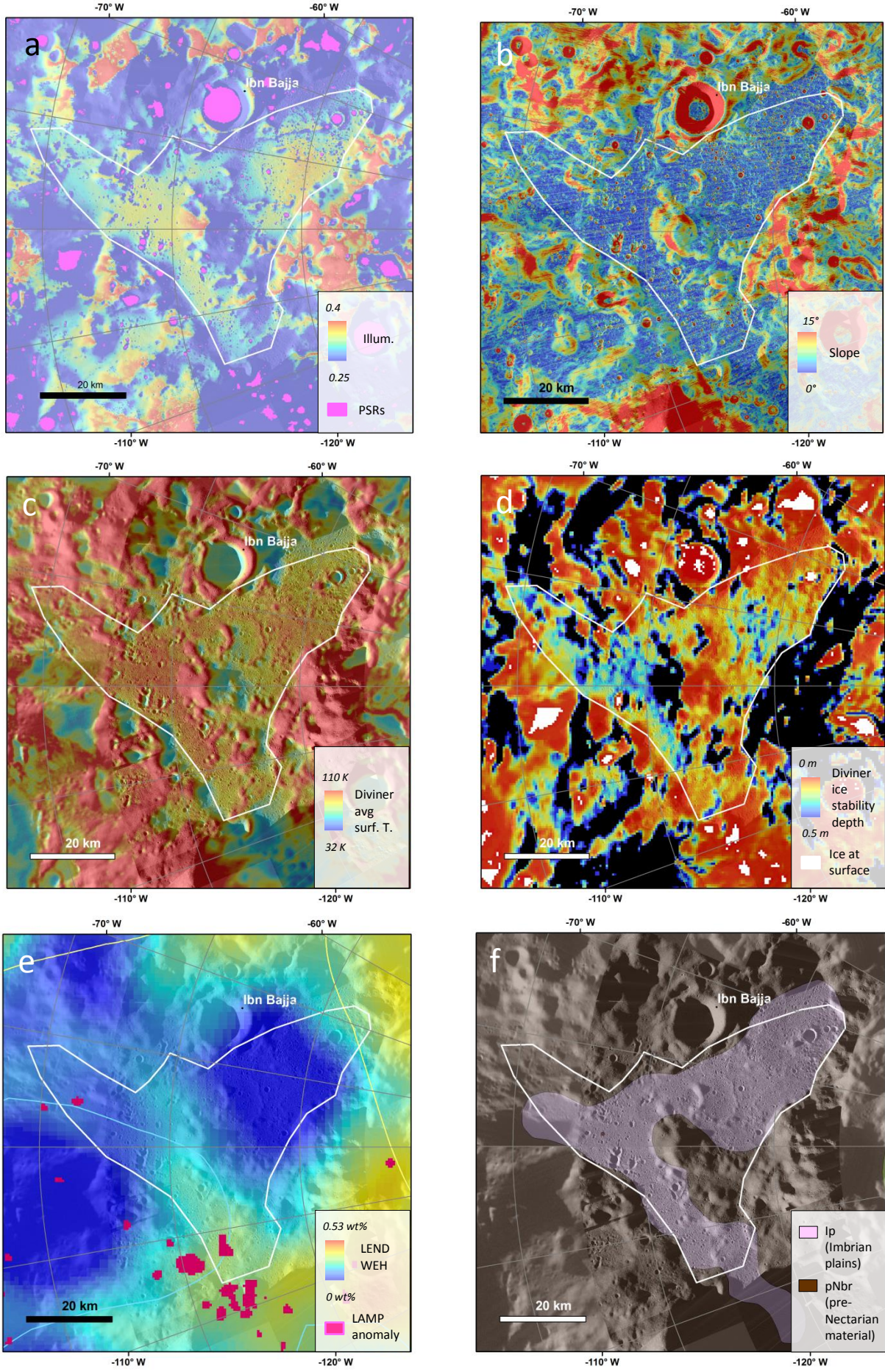


Figure 7

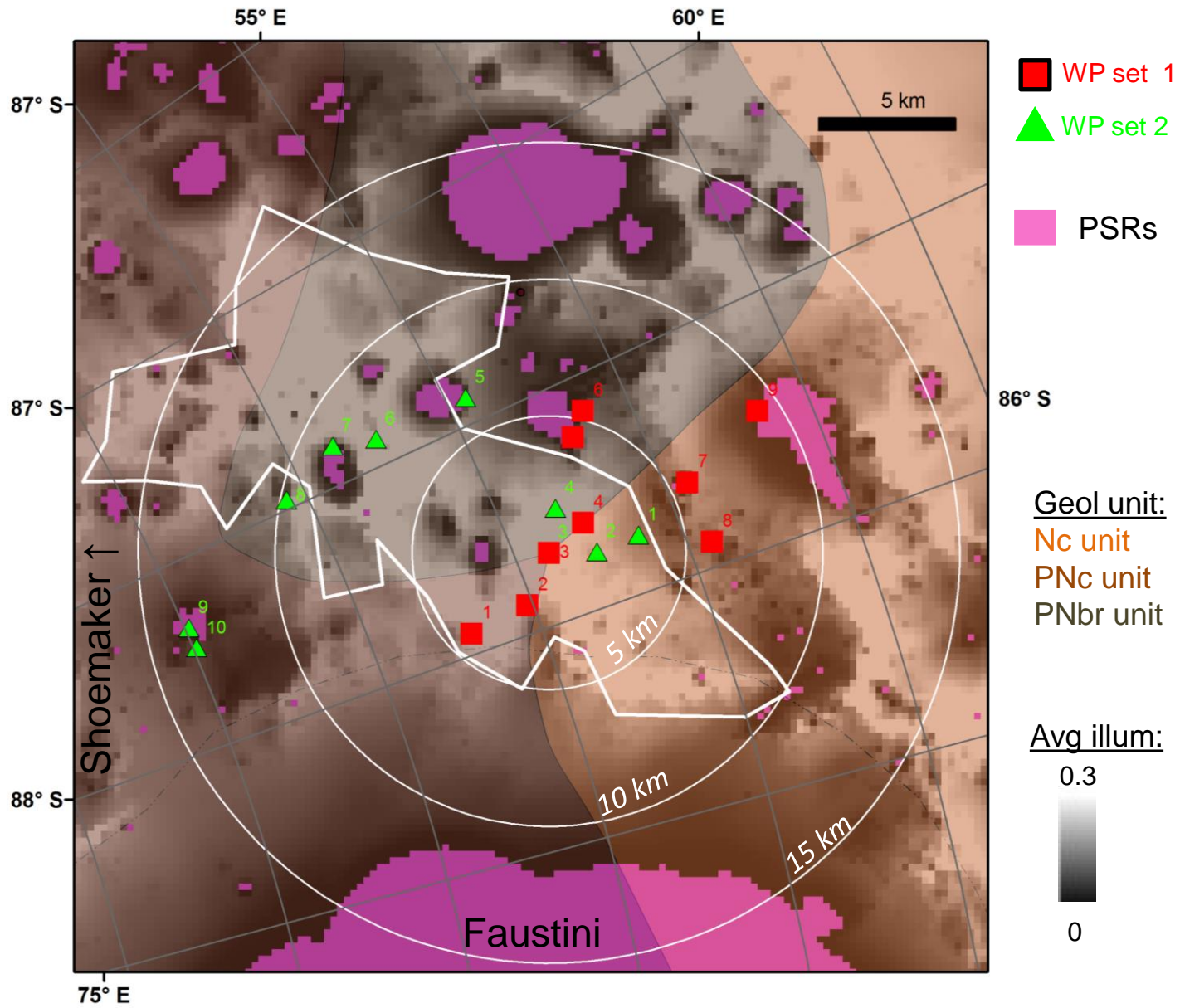


Figure 8

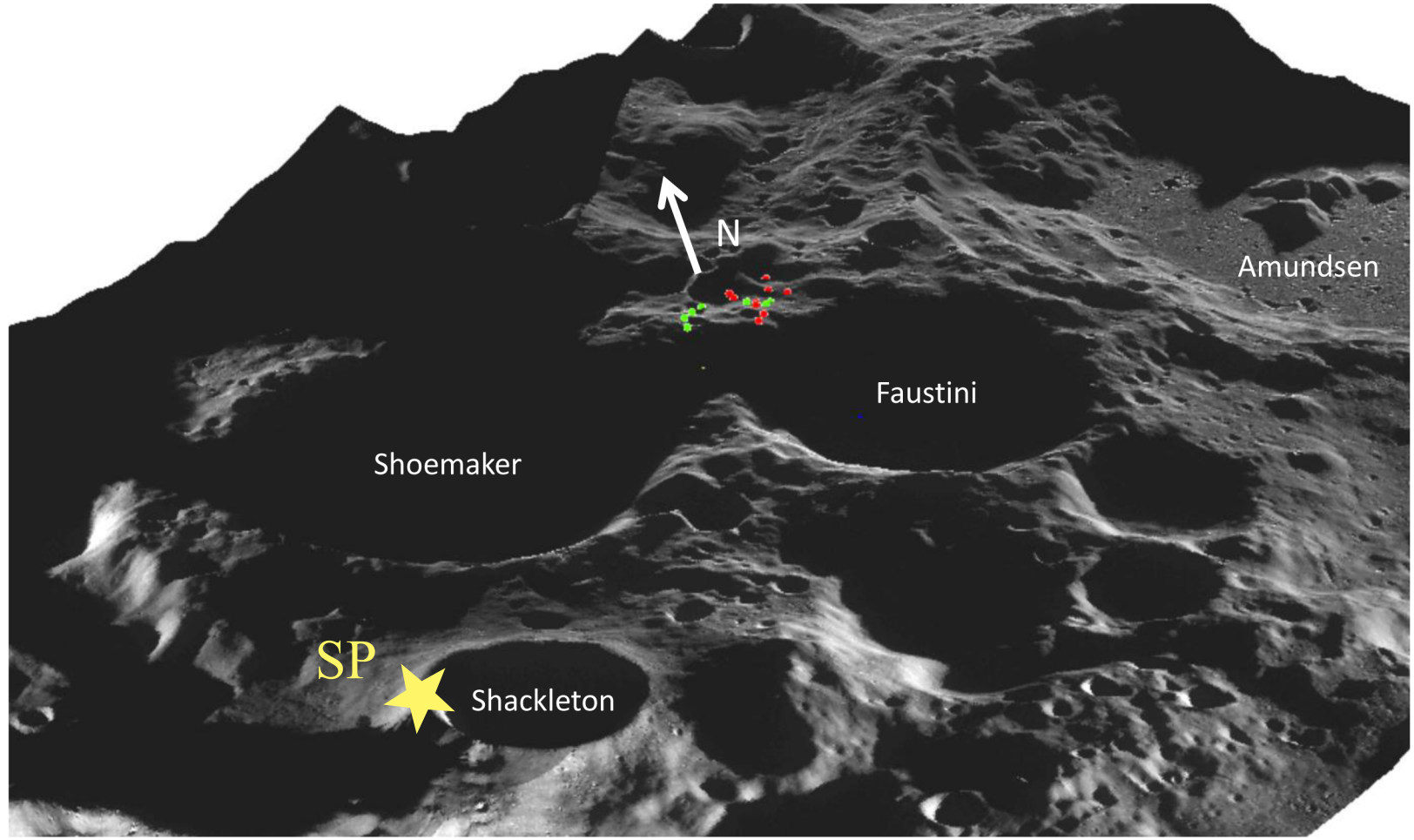


Figure S1

